Electrical operation of planar Ge hole spin qubits in an in-plane magnetic field

Sarkar, Abhikbrata; Wang, Zhanning; Rendell, Matthew; Hendrickx, Nico W.; Veldhorst, Menno; Scappucci, Giordano; Khalifa, Mohammad; Salfi, Joe; Saraiva, Andre; More Authors

DOI
10.1103/PhysRevB.108.245301

Publication date
2023

Document Version
Final published version

Published in
Physical Review B

Electrical operation of planar Ge hole spin qubits in an in-plane magnetic field

Abhikbrata Sarkar,[1] Zhanning Wang,[1] Matthew Rendell,[1] Nico W. Hendrickx,[2] Menno Veldhorst,[2] Giordano Scappucci,[2] Mohammad Khalifa,[3,4] Joe Salfi,[3,4] Andre Saraiva,[5] A. S. Dzurak,[5] A. R. Hamilton,[1] and Dimitrie Culcer[1]

[1]*School of Physics, The University of New South Wales, Sydney 2052, Australia*

[2]*QuTech and Kavli Institute of Nanoscience, Delft University of Technology, 2628 CJ Delft, The Netherlands*

[3]*Department of Electrical and Computer Engineering, University of British Columbia, Vancouver, B.C. V6T 1Z4, Canada*

[4]*Quantum Matter Institute, University of British Columbia, Vancouver, B.C. V6T 1Z4, Canada*

[5]*School of Electrical Engineering and Telecommunications, The University of New South Wales, Sydney 2052, Australia*

(Received 3 July 2023; revised 21 October 2023; accepted 23 October 2023; published 4 December 2023)

Hole spin qubits in group-IV semiconductors, especially Ge and Si, are actively investigated as platforms for ultrafast electrical spin manipulation thanks to their strong spin-orbit coupling. Nevertheless, the theoretical understanding of spin dynamics in these systems is in the early stages of development, particularly for in-plane magnetic fields as used in the vast majority of experiments. In this work, we present a comprehensive theory of spin physics in planar Ge hole quantum dots in an in-plane magnetic field, where the orbital terms play a dominant role in qubit physics, and provide a brief comparison with experimental measurements of the angular dependence of electrically driven spin resonance. We focus the theoretical analysis on electrical spin operation, phonon-induced relaxation, and the existence of coherence sweet spots. We find that the choice of magnetic field orientation makes a substantial difference for the properties of hole spin qubits. Specifically, we find that (i) EDSR for in-plane magnetic fields varies nonlinearly with the field strength and weaker than for perpendicular magnetic fields. (ii) The EDSR Rabi frequency is maximized when the a.c. electric field is aligned parallel to the magnetic field, and vanishes when the two are perpendicular. (iii) The orbital magnetic field terms make the in-plane g-factor strongly anisotropic in a squeezed dot, in excellent agreement with experimental measurements. (iv) Focusing on random telegraph noise, we show that the effect of noise in an in-plane magnetic field cannot be fully mitigated, as the orbital magnetic field terms expose the qubit to all components of the defect electric field. These findings will provide a guideline for experiments to design ultrafast, highly coherent hole spin qubits in Ge.

DOI: 10.1103/PhysRevB.108.245301

I. INTRODUCTION

Solid state spin qubits are prime candidates for scalable, highly coherent quantum computing platforms [1–9]. Among these group IV materials such as Ge and Si stand out thanks to the absence of piezoelectric interaction with phonons [10] and the possibility of isotopic purification, which eliminates the contact hyperfine coupling to the nuclear field [11,12], with the maturity of semiconductor microfabrication as an added advantage. Recent years have witnessed a concerted push towards all-electrical qubit operation, since electric fields are easier to apply and local ize than magnetic fields, and electrically operated qubit gates offer significant improvements in speed and power consumption as compared to magnetic gates. A series of theoretical predictions [13–16] as well as experimental leaps in growth techniques and sample quality [17–19] have led to a surge in interest in spin-3/2 hole systems in group IV materials. The strong and multifaceted spin-orbit coupling experienced by holes [10,20–24], their anisotropic and tunable g-tensor [25–29], and the absence of a valley degree of freedom makes them ideal for electrical spin manipulation, with Ge offering the additional advantages of a small effective mass [30] and ease of ohmic contact formation. Compared to electrons, the weaker hyperfine coupling for holes [31,32] due to the absence of the contact interaction significantly reduces the nuclear field contribution to spin decoherence, while the hole spin-3/2 is responsible for physics with no counterpart in electron systems [21,33–36], which may offer flexibility in future design strategies—for example magic angles have been predicted for acceptor qubits, [35] at which dipole-dipole entanglement can be switched off without switching off the electric dipole moments of single qubits.

Remarkable progress on hole spin qubits in several architectures has spanned more than a decade, with an overwhelming focus on Ge and Si [7–9]. Initial work focused on measuring hole spin states [37–40], relaxation and dephasing times [41–43], single spin electrical control [44], readout and control of the g-tensor [45–55] and of spin states in multiple dots [39,56–59], and achieving single-spin spin qubits. [60,61] In recent years the development of strained germanium in SiGe heterostructures [19,30,62] provided a low-disorder environment, which supported the development of single-hole qubits [63], singlet-triplet qubits [64], universal quantum logic [65], and a four-qubit germanium quantum processor [66]. Experiments have demonstrated ultrafast spin manipulation using the spin-orbit interaction [63,65,67,68] and EDSR Rabi oscillations as fast as 540 MHz [68], electrical control of the underlying spin-orbit coupling [69,70] and charge sensing using a superconducting resonator [71],

while relaxation times of up to 32 ms have been measured in Ge dots [72]. Hole spins in Ge have been used as quantum simulators [73] and control of an array of 16 Ge hole dots has been demonstrated [74]. The development of hybrid structures offers another path towards entanglement, with the demonstrations of superconductivity in planar Ge, [75–77] hole coupling to a superconducting resonator [78], dipole coupling to a microwave resonator [79], charge sensing using a superconducting resonator [71] and devices such as transistors and interferometers [80]. Theoretically, the interplay of spin-orbit coupling and superconductivity in hybrid semiconductor-superconductor structures is only now being studied in the context of quantum computing [81].

Concomitantly, Si qubits have also registered remarkable recent progress, with coherence times of up to 10ms in Si:B acceptors [82] and the detection of sweet spots as a function of the top gate field in quantum dots [83], sweet spots having been the subject of a number of theoretical studies [14,30,35,52,84–91]. Anisotropic exchange was also used to entangle two hole qubits [92], hole coupling to a superconducting resonator has been demonstrated [93], and progress has been made towards higher-temperature operation with the observation of Coulomb diamonds up to 25 K [94] and single-qubit operation above 4 K [95].

Despite experimental advances on many fronts, constructing an all-encompassing theory to describe hole physics in group-IV semiconductor quantum dots is challenging. In particular, owing to different effective masses and intrinsic spin-orbit gap in the valence band of these materials, the wide range of QD sizes as well as spin manipulation timescales exhibited in experiments render it difficult to provide a theory of spin qubits common to Si and Ge. In this work we will focus on Ge, which is somewhat more tractable analytically than Si, and describe electrical qubit operation in an in-plane magnetic field. This choice is motivated by the observation that experiments has overwhelmingly favoured in-plane magnetic fields [61,63], partly because a transverse magnetic field makes it easier to suppress hyperfine and cyclotron quantization effects, and partly in order to avoid the strong orbital coupling of the perpendicular field, which can cause a large diamagnetic shift and also affect tunnel rates. For spin-3/2 holes, in-plane magnetic fields are highly nontrivial, because the spin and orbital degrees of freedom are intertwined. The in-plane g-factor is very small, and in Ge most of it comes from the octupole interaction with the magnetic field [96]. Whereas in-plane magnetic fields have been considered for realistic devices in recent theoretical studies [90,97–99], these efforts have been largely from an engineering point of view, and the orbital effect of an in-plane magnetic field in planar quantum dots has largely been neglected, though they have been shown to play an important role in nanowires [100,101]. It has thus not been possible to date to construct a full picture of spin dynamics and electrical spin operation in planar Ge hole dots in an in-plane magnetic field. This has left several outstanding questions unanswered: *what determines the speed of EDSR, as well as the relaxation time T_1? Is there an optimal magnetic field orientation for driving a spin-orbit qubit? Do coherence sweet spots exist when the magnetic field is in the plane?*

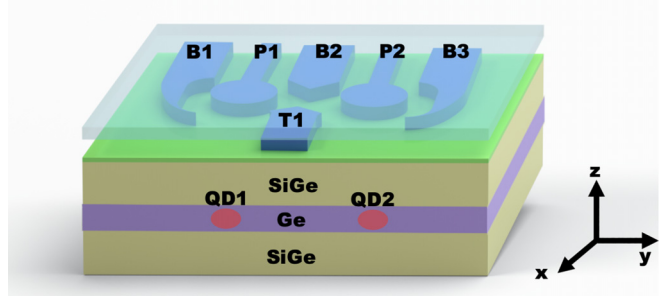

FIG. 1. A prototype double quantum dot in a strained germanium hole system. The strained quantum well is grown epitaxially on a strain-relaxed SiGe layer. Gate B2 and T1 control the inter-dot tunneling. The growth direction is $\hat{z}$.

In this work we seek to answer these questions. Our focus will be on gate-defined Ge quantum dots, with the parent 2DHG exhibiting very high mobility[18,102], low percolation density, [62,103], and a low effective mass of $m_h = 0.05\, m_e$ [19,75], which all aid the formation of quantum dots. One reason for our choice of Ge is its band alignment, which makes it the only group IV material suitable for growing quantum wells. Another reason is pragmatic—it is easier to describe theoretically. This is because the spin-orbit splitting in Ge ($\Delta_{\rm SO} = 325$ meV) is stronger than that in Si ($\Delta_{\rm SO} = 44$ meV), resulting in a large separation of the spin-orbit/split-off (SO) band from the heavy- and light-hole subspaces. This ensures that the 4×4 Luttinger Hamiltonian formalism for spin-3/2 is adequate for the topmost Ge valence band, as opposed to Si where the Rashba mediated electrical control features both heavy hole-light-hole (HH-LH) coupling contributions and heavy hole-split off (HH-SO) coupling contributions. Ge has a noticeable cubic-symmetry contribution to the Luttinger Hamiltonian. It is strong enough to enable electrical spin manipulation in planar dots [30,87], making Ge ideal for electrical spin operation, but not as strong as in Si, such that it can be treated perturbatively.

Figure 1 provides a schematic of the device architecture for studying a planar germanium hole quantum dot qubit. In this paper we concentrate on developing the key formalisms for describing the spin physics of hole spin qubits in an in-plane magnetic field. To avoid unneccessary complexity, and to keep our results generally applicable, we avoid making the analysis overly device specific; therefore we do not consider effects of gate electrode induced nonuniform strain which can lead to a significant modification of the spin-orbit interaction [55,104]; or Fowler-Nordheim tunneling of hole states through the SiGe barrier leading to charge accumulation at the interface between the semiconductor and the gate dielectric; or light-hole penetration through the SiGe barrier. Addressing these would require detailed finite element numerical simulation techniques on top of the theory developed here.

For an applied in-plane magnetic field operation of planar Ge hole QD, in the presence of uniaxial strain but neglecting shear strain, we show that: (i) EDSR is linear in the magnetic field with nonlinear corrections emerging at larger fields, and is driven by Rashba spin-orbit coupling rather than by the orbital magnetic field terms; the picture that emerges is that

the orbital B terms give rise to the finite Zeeman splitting between the qubit energy levels, while the Rashba spin-orbit coupling gives rise to transitions between them. The EDSR Rabi frequency is a maximum when the ac electric field is parallel to the magnetic field, and vanishes when the two are perpendicular; it can be sizable despite the smallness of the in-plane g-factor, and has a nonmonotonic dependence on B. (ii) The relaxation rate is due to bulk acoustic phonons and is proportional to B^3 in the leading power [105]. (iii) For a squeezed (elliptical) dot with an aspect ratio $L_y/L_x = 2$ the spin-flip frequency is an order of magnitude faster than for a circular dot allowing Rabi time $\sim$10 ns with $\sim 10^5$ operations within time T_1. (iv) For a squeezed dot, due to the effect of the orbital vector potential terms, the in-plane g-factor exhibits a strong anisotropy resulting in oscillatory behavior as the magnetic field is rotated in the plane of the dot, an observation supported by new experimental measurements shown in Sec. V of this paper. (v) Although extrema in the qubit Zeeman splitting as a function of the top gate voltage exist in the same way as for a perpendicular magnetic field [87], the effect of random telegraph noise in an in-plane magnetic field cannot be entirely mitigated, because the vector potential terms expose the qubit to all components of a defect's electric field.

The outline of this paper is as follows. Section II lays down the foundation of the numerical model of a Ge hole quantum dot qubit withing the framework of effective mass theory. Next we discuss the properties of circularly symmetric dots in Sec. III, including the qubit Zeeman splitting, EDSR, relaxation, and dephasing. In Sec. IV, we focus on elliptical dots and study their EDSR and coherence properties, while in Sec. V, we discuss the consequences of g-factor anisotropy and compare our predictions with recent experimental results. We end with a summary and outlook in Sec. VI.

II. HAMILTONIAN AND MODEL

The topmost valence band in Ge has orbital angular momentum $l = 1$. When the hole spin $s = 1/2$ is taken into account the resultant states at the $\mathbf{\Gamma}$-point are eigenstates of the total angular momentum $\mathbf{J} = (\mathbf{L} + \mathbf{S})$. The fourfold degenerate $j = 3/2$ states are separated by the spin-orbit gap Δ_0 from the $j = 1/2$ twofold degenerate split-off states. For Ge the spin-orbit gap $\Delta_0 = 325$ meV, so the split-off band is safely disregarded in describing hole motion in the topmost valence bands. The $|\frac{3}{2}\rangle$ and $|-\frac{3}{2}\rangle$ states constitute the heavy-hole (HH) manifold while the $|\frac{1}{2}\rangle$ and $|-\frac{1}{2}\rangle$ states represent the light-hole (LH) manifold. The Luttinger Hamiltonian describes the hole motion in the topmost valence bands and has the following form in the $j = 3/2$ basis $\{|\frac{3}{2}\rangle, |-\frac{3}{2}\rangle, |\frac{1}{2}\rangle, |-\frac{1}{2}\rangle\}$:

$$H_{\mathrm{LK}}(k) = \begin{pmatrix} P'+Q' & 0 & L' & M' \\ 0 & P'+Q' & M'^{*} & -L'^{*} \\ L'^{*} & M' & P'-Q' & 0 \\ M'^{*} & -L' & 0 & P'-Q' \end{pmatrix}, \quad (1)$$

where the matrix elements of the Luttinger Hamiltonian comprise the k-dependent part and strain-induced perturbations: $P' = P(\mathbf{k}) + P_\varepsilon$, $Q' = Q(\mathbf{k}) + Q_\varepsilon$, $L' = L(\mathbf{k}) + L_\varepsilon$, $M' = M(\mathbf{k}) + M_\varepsilon$. The kinetic energy terms are $P = \frac{\hbar^2\gamma_1}{2m_0}(k_x^2 + k_y^2 + k_z^2)$, $Q = \frac{\hbar^2\gamma_2}{2m_0}(k_x^2 + k_y^2 - 2k_z^2)$, $L = \frac{-\sqrt{3}\hbar^2\gamma_3}{m_0}(\{k_x, k_z\} - i\{k_y, k_z\})$ and $M = \frac{\sqrt{3}\hbar^2}{2m_0}\{-\gamma_2(k_x^2 - k_y^2) + 2i\gamma_3\{k_x, k_y\}\}$. The strain terms are: $P_\varepsilon = -a(\varepsilon_{xx} + \varepsilon_{yy} + \varepsilon_{zz})$, $Q_\varepsilon = -b(\varepsilon_{xx} + \varepsilon_{yy} - 2\varepsilon_{zz})$, $L_\varepsilon = d(\varepsilon_{xz} - i\varepsilon_{yz})$ and $M_\varepsilon = \frac{\sqrt{3}}{2}b(\varepsilon_{xx} - \varepsilon_{yy}) - d\varepsilon_{xy}$. Here m_0 is the bare electron mass while $\gamma_1 = 13.35$, $\gamma_2 = 4.25$, and $\gamma_3 = 5.69$ are Luttinger parameters for Ge. The constant $a = 2$ eV is the hydrostatic deformation potential, $b = -2.16$ eV is the uniaxial deformation potential, and $d = -6.06$ eV accounts for the shear deformation potential. In most Ge/GeSi samples there is considerable strain in the quantum well, which significantly increases the splitting between light and heavy holes compared to silicon—here we take the compressive strain to be 0.6% [18]. The strain tensor components in the plane are: $\varepsilon_{xx} = \varepsilon_{yy} = -0.006$. The in-plane compressive strain elongates the out-of-plane lattice constant via $\varepsilon_{zz} = -2\frac{C_{12}}{C_{11}}\varepsilon_{xx} = 0.004$; with $C_{12} = 44$ GPa, $C_{11} = 126$ GPa [106]. We assume the off-diagonal shear elements of the strain tensor to be $\varepsilon_{ij|_{i\neq j}} = 0$. The out-of-plane confinement is described by a one-dimensional infinite square well potential

$$V(z) = \begin{cases} \infty & z \in \left\{-\frac{L_z}{2}, \frac{L_z}{2}\right\} \\ 0 & \text{otherwise} \end{cases}. \quad (2)$$

The coupling to the top-gate electric field, denoted by F_z, gives an additional term $eF_z z$ in the Hamiltonian. The in-plane confinement is modelled by a parabolic potential $V_{x,y} = \frac{1}{2}(\lambda_x^2 x^2 + \lambda_y^2 y^2)$, where λ_x, λ_y are determined by the dot dimensions L_x, L_y in the plane. The effective hole QD Hamiltonian is given by

$$H_{0D} = H_{\mathrm{LK}}(\mathbf{k}) + eF_z z + V_{\mathrm{conf}}, \quad (3)$$

where $V_{\mathrm{conf}} = V_{x,y} + V(z)$ is the total confinement potential. The Zeeman interaction is given by

$$H_Z = -2\kappa\mu_B \mathbf{B}\cdot\mathbf{J} - 2q\mu_B \mathbf{B}\cdot\mathcal{J}, \quad (4)$$

where $\mathbf{J} = \{J_x, J_y, J_z\}$, $\mathcal{J} = \{J_x^3, J_y^3, J_z^3\}$; and J_x, J_y, J_z are the 4×4 Pauli matrices. μ_B is the Bohr magneton; and $\kappa = 3.41$, $q = 0.07$ for Ge signify the bulk g-factors of isotropic and anisotropic Zeeman interactions respectively. The $\mathcal{J}$-terms are vital in order to obtain the correct in-plane g-factor $\approx$0.25.

In the presence of a magnetic field, the canonical momentum of holes in topmost valence band becomes $\mathbf{k} \to (\mathbf{k} + \frac{e\mathbf{A}}{\hbar})$. The hole spin in a planar Ge quantum dot is then described by

$$H_{QD} = H_{\mathrm{LK}}\left(\mathbf{k} + \frac{e\mathbf{A}}{\hbar}\right) + eF_z z + V_{\mathrm{conf}} + H_Z. \quad (5)$$

The resultant modifications due to the vector potential $\mathbf{A}$ in $H_{\mathrm{LK}}(\mathbf{k} + \frac{e\mathbf{A}}{\hbar})$ lead to nontrivial contributions to the effective spin-orbit interaction in the HH and LH manifolds, subsequently labeled as "orbital $\mathbf{B}$ terms." To check the gauge invariance of our theoretical framework, we consistently diagonal ize the effective quantum dot Hamiltonian using two

different gauges:

(1) $\mathbf{A} = -\frac{1}{2}B_z y\hat{\mathbf{e}}_\mathbf{x} + \frac{1}{2}B_z x\hat{\mathbf{e}}_\mathbf{y} + (B_x y - B_y x)\hat{\mathbf{e}}_\mathbf{z}$;

(2) the symmetric gauge: $\mathbf{A} = \frac{1}{2}\mathbf{B}\times\mathbf{r} = \frac{1}{2}(B_y z - B_z y)\,\hat{\mathbf{e}}_\mathbf{x} + \frac{1}{2}(B_z x - B_x z)\,\hat{\mathbf{e}}_\mathbf{y} + \frac{1}{2}(B_x y - B_y x)\,\hat{\mathbf{e}}_\mathbf{z}$.

All calculations have been performed in both gauges, yielding consistent results (Appendix A).

The eigenstates of the hole QD can be expressed as linear combinations of states belonging to a basis in which the *bare* QD Hamiltonian is diagonal, i.e., $|\Psi_{QD}\rangle = \sum_i c_i\psi_i(x,y,z)|\phi_j\rangle$, where the *bare* Hamiltonian refers to H_{QD} of Eq. (5) with its off-diagonal elements set to zero, following the practice of $\boldsymbol{k}\cdot\boldsymbol{p}$ theory, as well as the external magnetic field set to zero. We choose the spatial wave functions as $\psi(x,y,z) = \psi_n(x)\,\psi_m(y)\,\psi_l(z)$, where the in-plane basis states are **1**-D Harmonic oscillator states for x and y and the out-of-plane basis states are given by solutions of the infinite potential well:

$$\psi_n(x) = \frac{1}{\sqrt{2^n\,n!}}\frac{1}{\sqrt{L_x\sqrt{\pi}}}e^{-\frac{x^2}{2L_x^2}}H_n\left(\frac{x}{L_x}\right),\ x\in\{-\infty,\infty\};$$

$$\psi_m(y) = \frac{1}{\sqrt{2^m\,m!}}\frac{1}{\sqrt{L_y\sqrt{\pi}}}e^{-\frac{y^2}{2L_y^2}}H_m\left(\frac{y}{L_y}\right),\ y\in\{-\infty,\infty\};$$

$$\psi_l(z) = \begin{cases}\cos\left(\frac{(l+1)\pi z}{L_z}\right) & l \text{ is even}\\ \sin\left(\frac{(l+1)\pi z}{L_z}\right) & l \text{ is odd}\end{cases}, z\in\left\{-\frac{L_z}{2},\frac{L_z}{2}\right\}. \quad (6)$$

The indices n, m, l in Eq. (6) can take integer values 0, 1, 2, 3, etc. The hole spinors represent the $j = 3/2$ spin states: $|\phi_j\rangle \in \{|\frac{3}{2}\rangle, |-\frac{3}{2}\rangle, |\frac{1}{2}\rangle, |-\frac{1}{2}\rangle\}$. When operated at low in-plane **B** we are in the $\omega_c \ll \omega_0$ limit, with ω_c the cyclotron frequency, so any effect of the in-plane magnetic field on the dot size are generally irrelevant (they are taken into account in our 3D formalism). This means the Fock-Darwin solutions have a one-on-one analogy to the harmonic oscillator solutions in Eq. (6). The in-plane basis states $\Psi_n(x)\Psi_m(y)$ are ordered according to their energy $\propto (n+m+1)$. We find converging solutions to Eq. (5) by considering 55 in-plane basis states, i.e., $(n+m)\in[0,9]$; and 15 out-of-plane $\Psi_l(z)$ basis states, i.e., $l\in[0,14]$. We note that the $(n+m)=0$ level has no degeneracy; but considering the degeneracies of $(n+m) = 1, 2, \ldots, 9$; the simulation spans 55 in-plane levels. The numerical diagonalization of the resultant 3300×3300 Hamiltonian yields the energy levels of the hole quantum dot: $H_{QD}|\Psi_{QD}\rangle = \lambda_E|\Psi_{QD}\rangle$.

We comment briefly on the choice of spatial Ge basis functions. Variational analyses of the z-wave function incorporating the top gate potential have successfully described Ge hole QDs in Refs. [23,87], but the variational model is hard to extend to a full 3D numerical analysis due to the complicated form of the variational excited states. For example, the Airy function [90,105] provides the exact solution if the z confinement is modelled as a triangular potential well but can yield a residual Rashba spin-orbit interaction at nonzero top gate potential ($F_z > 0$), requiring a careful choice and implementation of boundary conditions. In the present paper we describe the z confinement using an infinite square well augmented by a linear electrostatic potential that accounts for the top gate, and consider top gate fields up to 50MV/m (although values up to 100 MV/m can also be studied with this method). Ref. [90] used a sophisticated model that incorporates Fowler-Nordheim tunneling, which is beyond the scope of the present study, as explained below. We stress that the range of F_z is at the lower end of what we consider here (up to 2.5 MV/m), and thus our studies can be regarded as complementary.

When the out-of-plane confinement of the hole QD is much stronger than the in-plane confinement, i.e., in the quasi-2D limit, the energy splitting Δ_{HL} between the heavy-hole (HH) and the light-hole (LH) states becomes much larger than the in-plane confinement energy. In this situation, one can use quasidegenerate perturbation theory (the Schrieffer-Wolff transformation) to write an effective 2×2 Hamiltonian for the 2D hole gas. This approach, when applicable, is a useful complement to the numerical calculations, providing additional insight into physical processes and functional dependencies. For this purpose the HH-LH coupling terms, e.g., L, M of Eqs. (1)–(5) would be treated perturbatively—the details of the SW transformation are provided in supplementary information 2. The effective Hamiltonian has the following form:

$$H^{ij}_{\text{eff}} = H^{ij}_{QD} + \frac{1}{2}\sum_{m=3,4} H^{im}_{QD}H^{mj}_{QD}\left(\frac{1}{\Delta_{im}}+\frac{1}{\Delta_{jm}}\right)+\ldots, \quad (7)$$

where $i, j = 1, 2$. This picture can be useful for providing qualitative explanations of certain experimental observations. For example, recent experiments have shown unambiguously that the g-factor of a 2D hole gas is a strong function of density [52,107]. This is explained by effective 2D theoretical models [20,23,26,108], which show that the in-plane magnetic field gives rise to an effective spin-orbit coupling whose magnitude is proportional to B [20,26,108]. However, a significant degree of caution must be exercised when seeking to understand the dynamics of quantum dots in an in-plane magnetic field, where a naive application of quasidegenerate perturbation theory is insufficient. In general, the effective spin-orbit interaction due to the orbital magnetic field terms has a highly nontrivial interplay with the Rashba spin-orbit interaction stemming from the top-gate potential [20,96,108]. For a hole QD in an in-plane magnetic field, as considered here, this interplay results in significant contribution to hole spin dynamics from the orbital magnetic field terms. This contribution, as the following sections make clear, cannot be captured by a naive Schrieffer-Wolff transformation, because the orbital magnetic field terms couple the in-plane and out-of-plane dynamics in a way that makes them inseparable: if one first reduces the 3D Hamiltonian to an effective 2×2 Hamiltonian for a 2D hole gas, and then attempts to understand QD dynamics based on this effective 2D Hamiltonian (in analogy with electron systems) all the physics of the orbital magnetic field terms is lost. Hence the full 3D theoretical model described is essential to understand the full spin dynamics of a hole quantum dot in an in-plane magnetic field.

With this in mind, in the subsequent sections we analyze numerical results from the 3D model, while the 2D formalism will be used for pedagogical reasons where appropriate, in particular when it can provide a simple intuitive picture of the role of various spin-orbit interactions in hole spin dynamics.

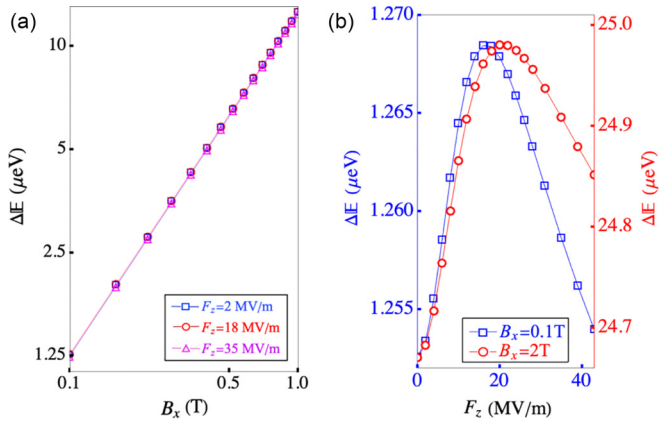

FIG. 2. Qubit Zeeman splitting of hole spin-qubit in $B_\parallel$. (a) Variation in the qubit Zeeman splitting $\Delta\mathbb{E}$ (μeV) with the in-plane magnetic field B_x(T). The Zeeman splitting shows a monotonic linear trend with B_x at $F_z = 2$ MV/m, $F_z = 18$ MV/m and $F_z = 35$ MV/m top-gate potentials respectively; with in-plane $g_\parallel \sim 0.22$. No significant difference occurs in the qubit Zeeman splitting for different top gate field. (b) The in-plane g-factor exhibits an extremum as a function of the top gate at $F_z = 18$ and 21 MV/m, respectively for $B_x = 0.1$ and 2 T.

III. CIRCULAR QUANTUM DOT

Qubit Zeeman splitting. We solve the full 3D Hamiltonian in an external magnetic field along x for a Ge hole QD with the following dimensions: $L_x = 50$ nm, $L_y = 50$ nm, and $L_z = 11$ nm. We evaluate the QD ground state $|\Psi_{GS}\rangle = \sum_i c_i\psi_i(x,y,z)|\phi_j\rangle$ and first excited state $|\Psi_{ES}\rangle = \sum_i c_i'\psi_i(x,y,z)|\phi_j\rangle$, labeling them as state $|\mathbb{0}\rangle$ with eigenenergy $\mathbb{E}_0$ and $|\mathbb{1}\rangle$ with eigenenergy $\mathbb{E}_1$, respectively. The coefficients $c_i(c_i')$ constitute the corresponding eigenvector to the eigenenergy $\mathbb{E}_0(\mathbb{E}_1)$. The strong z confinement and the compressive strain in the Ge layer governs the large heavy hole-light hole splitting of $\Delta_{LH} \sim 60$ meV, so that many in-plane (quantum dot) levels are contained between any two out-of-plane (quantum well) levels. This allows us to write the ground state and the first excited state as $|\pm\frac{3}{2}\rangle$ heavy hole-type with light-hole admixtures: $|\mathbb{0}\rangle = (c_1|0,0,0,\frac{3}{2}\rangle +$ admixtures) and $|\mathbb{1}\rangle = (c_1'|0,0,0,-\frac{3}{2}\rangle +$ admixtures), where the four indices denote n, m, l, J_z. This admixtures are determined by the two primary spin-orbit interactions in the system: structure inversion asymmetry (SIA) due to the top-gate potential F_z gives rise to the first Rashba term, which stems primarily from HH-LH coupling. The second contribution to the spin-orbit interaction comes from the orbital vector potential terms due to the in-plane magnetic field **B**. The qubit Zeeman splitting $\Delta\mathbb{E} = \mathbb{E}_1 - \mathbb{E}_0$ shows a linear trend with B_x [Fig. 2(a)], $\Delta\mathbb{E} = g_\parallel\mu_B B_x$, where the effective in-plane g-factor ranges between 0.215–0.219, expectedly ~3 orders of magnitude smaller than out-of-plane g-factor for Ge hole qubits; $g_\parallel \ll g_\perp$ [8]. The extrema in the qubit Zeeman splitting as a function of F_z in an in-plane **B** [Fig. 2(b)] are explained by the same mechanism as for out-of-plane magnetic field operation [87]. At small values of F_z the matrix elements connecting the HH and LH states, which give rise to Rashba spin-orbit coupling, increase linearly with the gate field, while the change in the HH-LH splitting is negligible. At large values of F_z the increase in the HH-LH splitting outweighs all other effects and the Rashba spin-orbit coupling decreases as a function of F_z. These competing effects give rise to an extremum in the qubit Zeeman splitting at a certain value of the top gate electric field, where the qubit is insensitive to z-electric field fluctuations.

EDSR. An alternating electric field $\tilde{\mathbf{E}}(t)$ can induce spin-flip transition between the primarily $|\pm\frac{3}{2}\rangle$-spin qubit states $|\mathbb{0}\rangle$ and $|\mathbb{1}\rangle$ via electron dipole spin resonance (EDSR). When the frequency of the ac electric field matches the Zeeman splitting of the hole spin qubit, $\Delta\mathbb{E} = h\nu$, i.e., at the resonance condition, the EDSR technique involves driving the hole spin via the second order virtual transition between the ground orbital state and excited orbital state of the QD.[30] The EDSR Rabi frequency is calculated as

$$f_{\text{EDSR}} = \langle\mathbb{0}|e\tilde{\mathbf{E}}(t)\cdot\mathbf{r}|\mathbb{1}\rangle. \tag{8}$$

Here we will focus on the scenario in which the alternating electric field is in the plane. For an applied oscillatory electric field of strength $E_0 = 10$ kV/m, Fig. 3(a) presents the spin-flip Rabi frequency variation w.r.t. the top gate field and applied B_x as calculated from the full 3D analysis, with the key features of the EDSR Rabi frequency exhibiting a maximum at a certain value of F_z, as well as a nonlinear dependence of f_{EDSR} on B_x. In figure 3, the nonlinearity of f_{EDSR} as function of the applied in-plane magnetic field B_x is best fit as $f_{\text{EDSR}} = a_f B_x + b_f B_x^2 + c_f B_x^3$ at a constant top gate field. We compare this result with the out-of-plane magnetic field operation of Ge hole qubits where f_{EDSR} shows linear trend with respect to $|B|$; explained by the effective 2D theory.[30,68,87] Following Eq. (7), we attempt to understand the f_{EDSR} vs B_x trend in this paper by calculating the effective 2D Hamiltonian in the $\{|\frac{3}{2}\rangle, |-\frac{3}{2}\rangle\}$ basis using the Schrieffer-Wolff transformation:

$$H_{\text{eff}}^{2\times2} = H_0 + H_{\text{SO}} + H_{Z,2\text{D}} + V(x,y) + eE_x(t)x,$$

where

$$H_0\left(\mathbf{k}_\parallel \to \left(\mathbf{k}_\parallel + \frac{e\mathbf{A}}{\hbar}\right)\right) = [\mathcal{A}k_\parallel^2 - \mathcal{B}k_\parallel^4 - D(k_+^2 - k_-^2)^2]I_{2\times2},$$

$$H_{\text{SO}} = \alpha_{R2}[k_+^3\sigma_- - k_-^3\sigma_+] - \alpha_{R3}[\{k_+^2, k_-\}\sigma_+ - \{k_+, k_-^2\}\sigma_-],$$

$$H_{Z,2\text{D}} = g_1\mu_B^3 B_x^3\sigma_x + g_2\mu_B B_x k_x^2\sigma_x + \frac{3}{2}q\mu_B B_x\sigma_x. \tag{9}$$

Here H_0 signifies the hole kinetic energy term in the 2D limit including a k^4 correction [96], and the D term represents warping of the energy contours [23]. We denote the in-plane wave vector as $\mathbf{k}_\parallel = k_x\hat{i} + k_y\hat{j}$, which satisfy $k_\parallel^2 = k_x^2 + k_y^2$, $k_\pm = k_x \pm ik_y$. The Pauli matrices satisfy $\sigma_\pm = \sigma_x \pm i\sigma_y$. The spin-orbit Hamiltonian H_{SO} comprises two important k-cubic Rashba terms induced by the top gate field; a spherical term $\propto\alpha_{R2}$ and a cubic-symmetric correction $\propto\alpha_{R3}$. The important Zeeman terms are listed in H_z; while the last two terms in $H_{\text{eff}}^{2\times2}$ represent the 2D confinement energy and the driving electric field applied along the x direction, respectively. The relevant coefficients of the effective 2D model are derived in supplementary information 2, while typical values of these parameters are provided in Tab. I.

The picture that emerges from the 2D model is the following: the orbital **B** terms along with the anisotropic Zeeman

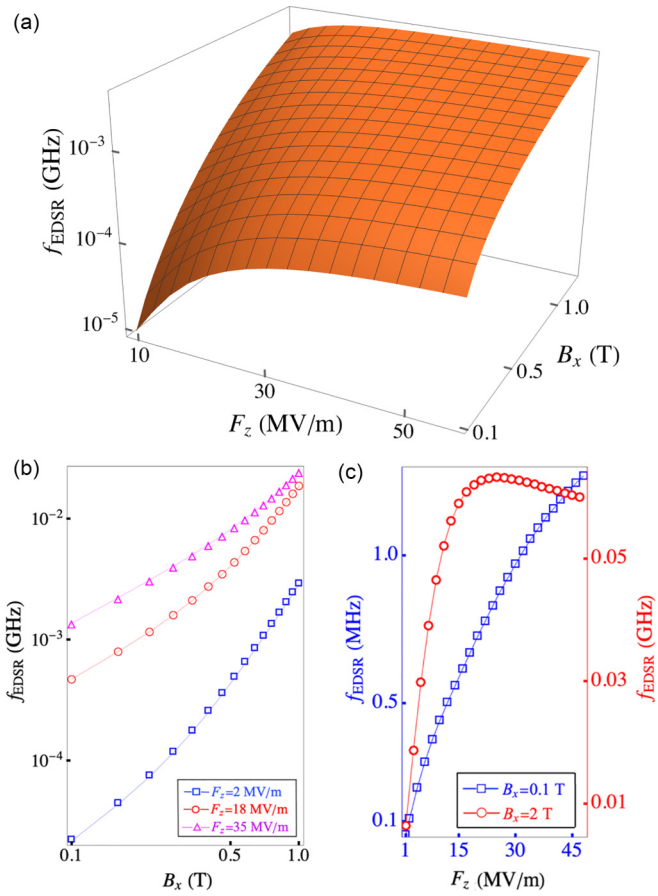

FIG. 3. Electric dipole spin resonance of hole qubit in $B_\parallel$. (a) Dependence of the EDSR Rabi frequency $f_{\rm EDSR}$(GHz) on the top gate field F_z(MV/m) and in-plane magnetic field $B_x(T)$. The strength of the in-plane EDSR driving ac electric field is $E_0 = 10$ kV/m. The z axis representing $f_{\rm EDSR}$ in the 3D plot is logarithmic. (b) Log-log plot of $f_{\rm EDSR}$ vs B_x showing a nonmonotonic dependence of EDSR Rabi frequency on the applied B field as $f_{\rm EDSR} = a_f B_x + b_f B_x^2 + c_f B_x^3$. The points on the plot signify results from the numerical calculation while the fitting is denoted by the dashed lines. At $F_z = 2$ MV/m, the fitting parameters are $a_f = 0.0002$, $b_f = 0.00002$, $c_f = 0.003$; at $F_z = 18$ MV/m they are $a_f = 0.005$, $b_f = 0.00006$, $c_f = 0.01$ and at $F_z = 35$ MV/m top-gate potential the fitting parameters are $a_f = 0.01$, $b_f = 0.00004$, $c_f = 0.01$. (c) The Rabi frequency exhibits maxima as a function of the top gate at $F_z = 18$ MV/m only for higher magnetic field ($B_x = 2$T), over the range of top-gate potentials used in this study.

interaction in H_Z give rise to a small finite spin splitting $\Delta\mathbb{E}$ in the lowest orbital state of the quantum dot. The driving term $eE_x(t)x$ generates a spin-preserving $\Delta n = 1$ orbital transition. The Rashba spin-orbit coupling $H_{\rm SO}$ gives rise to reversal of spin in the heavy hole manifold $|\frac{3}{2}\rangle \rightarrow |-\frac{3}{2}\rangle$, while inducing $\Delta n = 1$ transition between quantum dot orbital levels. Projecting $H_{\rm eff}^{2\times2}$ onto the in-plane quantum dot states, we evaluate the EDSR Hamiltonian in quasidegenerate perturbation theory as $H_Q = \frac{\Delta\mathbb{E}}{2}\sigma_z + hf_{\rm EDSR}\sigma_x$, with $f_{\rm EDSR} \propto B_x$ in the leading order, while the next order of expansion gives $f_{\rm EDSR} \propto B_x^3$ (Appendix B).

The significant quadratic B_x^2 dependence of the EDSR Rabi frequency at large F_z [Fig. 3(b)] is a signature of

TABLE I. Typical values of the 2D model parameters for hole number density of $p = 2 \times 10^{15}$ m^{-2} in the Ge quantum well (QW); which corresponds to a top gate field of $F_z \approx 2.5$ MV/m. The QW width is $L_z = 11$ nm.

effective 2D model parameters	value
hole number density in Ge layer, p	2×10^{15} m^{-2}
heavy hole-light hole splitting, Δ_{HL}	53.3 meV
$\mathcal{A}$	0.84 eV nm^2
$\mathcal{B}$	1.50 eV nm^4
$\mathcal{D}$	0.29 eV nm^4
α_{R2}	-0.09 eV nm^3
α_{R3}	0.01 eV nm^3
g_1	8.4×10^4 eV^{-2}
g_2	1.5×10^{-20} m^2

the orbital **B** terms. These terms couple the out-of-plane and in-plane hole dynamics, hence the resultant spin-orbit coupling is not fully captured by the effective 2D model. Using the full 3D analysis one can determine possible *paths* connecting the $|\mathbb{0}\rangle = (c_1|0,0,0,\frac{3}{2}\rangle + \text{admixtures})$ and $|\mathbb{1}\rangle = (c_1'|0,0,0,-\frac{3}{2}\rangle + \text{admixtures})$ qubit states. Choosing the symmetric gauge $\mathbf{A} = (0, -\frac{1}{2}B_x z, \frac{1}{2}B_x y)$, the orbital **B** terms induce the following transitions in the Luttinger-Kohn picture, e.g., $\{|\frac{3}{2}\rangle \xrightarrow{B_x} |\frac{1}{2}\rangle,\ |-\frac{1}{2}\rangle \xrightarrow{B_x} |-\frac{3}{2}\rangle\}$. The top gate potential gives $\{n_z \xrightarrow{eF_z z} n_z \pm 1\}$ which is spin conserving. The Luttinger terms $L(\mathbf{k})$, $M(\mathbf{k})$ couple HH and LH states, e.g., $\{|n_x, n_y, n_z, \frac{3}{2}\rangle \xrightarrow[L(\mathbf{k})]{k_x k_z} |n_x \pm 1, n_y, n_z \pm 1, \frac{3}{2}\rangle\}$. We consider the complete spin-orbit picture in the Ge hole QD following Eq. (5) to sketch a few example *paths* as follows:

(1) $|0,0,0,\frac{3}{2}\rangle \xrightarrow[L]{B_x} |0,0,0,\frac{1}{2}\rangle \xrightarrow[L]{k_y k_z} |0,1,1,\frac{3}{2}\rangle \xrightarrow[M]{k_x k_y}$
$|1,2,1,-\frac{1}{2}\rangle \xrightarrow{eF_z z} |1,2,0,-\frac{1}{2}\rangle \xrightarrow{eE_x x} |0,2,0,-\frac{1}{2}\rangle \xrightarrow[J\to J]{k_y^2}$
$|0,0,0,-\frac{1}{2}\rangle \xrightarrow[L]{B_x} |0,0,0,-\frac{3}{2}\rangle$.

(2) $|0,0,0,\frac{3}{2}\rangle \xrightarrow[L]{k_y k_z} |0,1,1,\frac{1}{2}\rangle \xrightarrow{eE_x x} |1,1,1,\frac{1}{2}\rangle \xrightarrow[J\to J]{B_x y k_z}$
$|1,0,2,\frac{1}{2}\rangle \xrightarrow{(eF_z z)^2} |1,0,0,\frac{1}{2}\rangle \xrightarrow[M]{k_x k_y} |0,1,0,-\frac{3}{2}\rangle \xrightarrow[J\to J]{B_x y k_z}$
$|0,0,1,-\frac{3}{2}\rangle \xrightarrow{eF_z z} |0,0,0,-\frac{3}{2}\rangle$.

These *paths* indicate the presence of an effective spin-flip matrix element between $|0,0,0,\frac{3}{2}\rangle \rightarrow |0,0,0,-\frac{3}{2}\rangle$ proportional to B_x^2. Figure 3(c) shows the variation of EDSR Rabi frequency with respect to the top gate field. At $B_x = 0.1$ T, $f_{\rm EDSR}$ increases slowly with the top gate field. On the other hand at higher magnetic fields ($B_x = 2$ T), the EDSR Rabi frequency increases more rapidly with F_z, and the maximum shifts towards lower values of F_z. We find $f_{\rm EDSR}$ to be a maximum when the ac electric field is parallel to the magnetic field, and vanishes when the two are perpendicular.

Phonon mediated relaxation. The relaxation mechanism in Ge hole QD qubits is well explained by acoustic phonon coupling to the hole spins through the valence band deformation potential $\mathcal{D}_{i,j}$ of Ge. There are no piezoelectric phonons in Ge, but the hole spin inter-

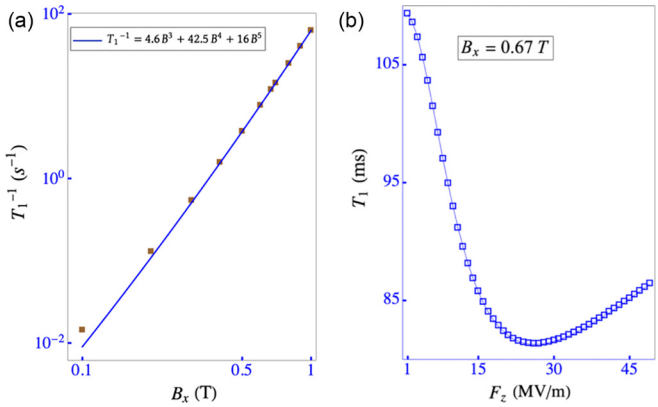

FIG. 4. Phonon induced hole spin-qubit relaxation for $B_\parallel$ operation. (a) Log-log plot of relaxation rate T_1^{-1} (s^{-1}) vs applied magnetic field B_x (T) at the top-gate field of $F_z = 18$ MV/m. The B dependence of the relaxation rate has been fitted using the fitting parameters shown in the top inbox. (b) The relaxation rate T_1^{-1} vs the top gate field F_z (MV/m) for $B_x = 0.67$ T.

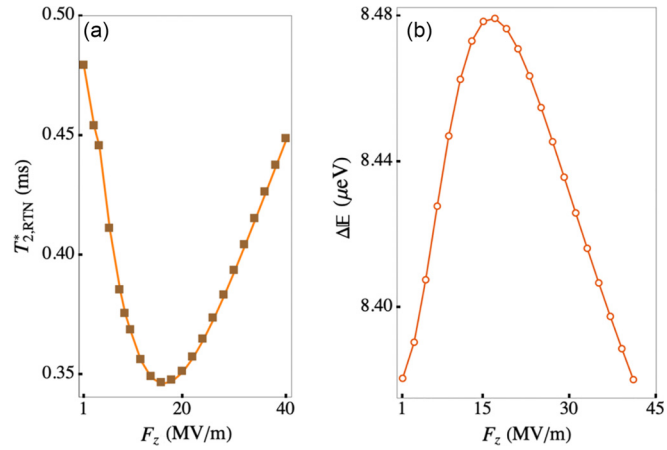

FIG. 5. Qubit dephasing in an in-plane magnetic field. (a) Variation of qubit dephasing time $T^*_{2,\mathrm{RTN}}$ (ms) due to random telegraph noise (RTN) from a nearby in-plane single charge defect 200 nm away from the qubit with respect to top gate field F_z (MV/m). (b) Qubit Zeeman splitting ΔE (μeV) vs applied top-gate field F_z (MV/m). The applied magnetic field is in the plane with the magnitude $B_x = 0.67$ T. The dephasing time reaches a minimum at $F_z = 18$ MV/m.

acts with the thermal bath of the bulk phonons via the hole-phonon Hamiltonian $H_{h-\mathrm{ph}}$, where $\alpha \in \{l, t, w\}$ denotes the polarization directions of the phonon and $\mathbf{q}$ is the phonon wave vector. We write $H_{h-\mathrm{ph}} = \sum_{i,j} \mathcal{D}_{i,j}\varepsilon^\alpha_{i,j}(\boldsymbol{r})$ with $\varepsilon^\alpha_{i,j}(\boldsymbol{r}) = \sum_q \frac{i}{2}\sqrt{\frac{\hbar}{2\rho N V \omega_{\mathbf{q},\alpha}}}(q_i\hat{c}_j + q_j\hat{c}_i)e^{i\mathbf{q}\cdot\boldsymbol{r}}\sqrt{N^\alpha_q + 1}$. The relaxation rate $1/T_1$ is written as

$$\frac{1}{T_1} = \frac{2\pi}{\hbar}\sum_{\alpha,\mathbf{q}} |\langle \mathbb{0}|H_{h-\mathrm{ph}}|\mathbb{1}\rangle_\alpha|^2 \delta(\Delta\mathbb{E} - \hbar\omega_{\alpha,\mathbf{q}}) \tag{10}$$

We calculate the relaxation rate using the full 3D quantum dot analysis by computing in real space the overlap integral $\langle \mathbb{0}|H_{h-\mathrm{ph}}|\mathbb{1}\rangle_\alpha$ due to position-dependent local strain, followed by the scattering integral in the phonon wave vector q-space for a specific polarization direction. The full analytical integrations and dipole approximation calculations are detailed in Appendix C. Figure 4(a) shows the nonlinear variation of the relaxation rate T_1^{-1} with respect to the external magnetic field B_x, where B^3, B^4 and B^5 terms present in the fitting are obtained from the full 3D numerical model. While the B^3 and B^5 dependencies are explained from the first two terms in the dipole approximation, the B^4 term is understood from the orbital B admixture. A minimum relaxation time $T_1 \sim 80$ ms at an in-plane magnetic field $B_x = 0.67$ T is obtained. This result from the theory compares well with a single hole relaxation time measurement in Ge of over 30 milliseconds and a five-hole relaxation time of approximately 1 millisecond by Lawrie *et al.* [72]. The magnetic field in the experimental setup [63,72] is $B = 0.67$ T, as also used in Fig. 4(a). There exists a minimum in T_1 in the range of F_z considered here for $B_x = 0.67$ T [Fig. 4(b)]. At this minimum the Rabi ratio $T_1/T_\pi \approx 2 \times 10^5$, where T_π is the time required for an EDSR π rotation, demonstrating that fast Rabi oscillations can be achieved without sacrificing T_1.

Random telegraph noise (RTN) dephasing. The large spin-orbit coupling exposes the hole spin qubit to charge noise. The dephasing time $T^*_{2,\mathrm{RTN}}$ is evaluated from the fluctuation in the qubit energy gap, denoted by $\delta\omega$, caused by the screened potential $U_s(\boldsymbol{r})$ of a nearby single charge defect in the 2DHG [91,109–112]. The mathematical formulation of $U_s(\boldsymbol{r})$ is given in Appendix D. The matrix elements $\langle n, m, l|U_s(\boldsymbol{r})|n', m', l'\rangle$ are added to the full Hamiltonian, and the 3300 × 3300 matrix is diagonal ized to evaluate the qubit energy splitting in the presence of the charge defect as $\Delta\mathbb{E} + \delta\omega$. The dephasing rate is

$$(T^*_{2,\mathrm{RTN}})^{-1} = \frac{(\delta\omega)^2\tau}{2\hbar^2}, \tag{11}$$

where the defect switching time is taken as $\tau = 10^3\, t_{\mathrm{Rabi}}$. This picture assumes the most significant contribution to RTN comes from charge defects away from the top gate, close to the qubit plane; hence we consider a single charge defect in the qubit plane situated 200 nm away from the center of the qubit. Fluctuating single charge defects right above the qubit will be screened by the presence of the top-gate, where the image charge changes the interaction to a much weaker dipole interaction. In contrast fluctuating charges in the plane of the quantum well are less effectively screened by surface gates, and may be the dominant source of charge noise [113].

It is evident that for hole qubit in an in-plane magnetic field, the dephasing time $T^*_{2,\mathrm{RTN}}$ actually decreases as a function of the top gate electric field F_z, and reaches a minimum at a certain value of this field [Fig. 5(a)], in other words, a coherence hot spot. The location of this dephasing time hotspot is closely related to the extremum in the qubit Zeeman splitting [Fig. 5(b)]. This behavior is in sharp contrast to hole spin qubits in a perpendicular magnetic field, where the qubit exhibits a sweet spot at a certain value of the top gate field [Fig. 6(a)], at which its sensitivity to noise vanishes to leading order in the noise strength, and dephasing time $T^*_{2,\mathrm{RTN}}$ reaches a maximum. The location of the sweet spot in F_z for out-of-plane qubit operation is closely related to an extremum in the qubit Zeeman splitting [Fig. 6(b)].

$B_\perp$ vs $B_\parallel$ coherent qubit operation. In the context of qubit coherence one must distinguish between extrema in the qubit

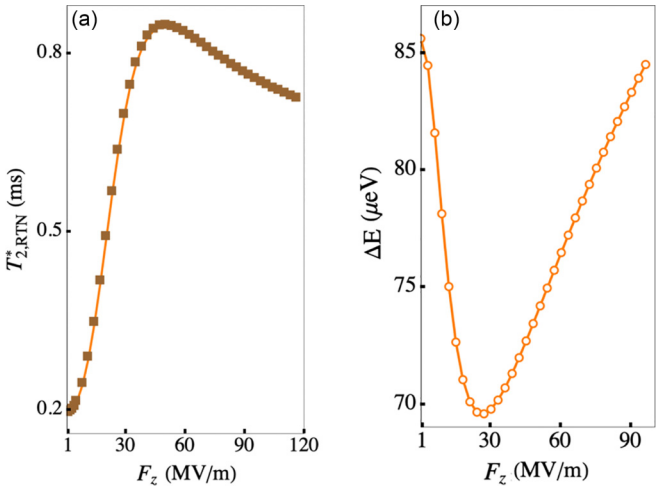

FIG. 6. Qubit dephasing in an out-of-plane magnetic field. (a) Variation of qubit dephasing time $T^*_{2,\mathrm{RTN}}$ (ms) due to random telegraph noise (RTN) from a nearby in-plane single charge defect 200 nm away from the qubit with respect to top gate field F_z (MV/m). (b) Qubit Zeeman splitting ΔE (μeV) vs applied top-gate field F_z (MV/m). The applied magnetic field is in the plane with the magnitude $B_x = 0.1$ T. In this case, the dephasing time exhibits a maximum in top-gate field.

Zeeman splitting and actual sweet spots in the coherence time. It is important to recall that in a spin qubit the dephasing time T_2^* depends on the magnitude of the magnetic field. This follows from time-reversal symmetry considerations, since the combination of charge noise and spin-orbit coupling cannot give rise to an energy difference between qubit states that form a Kramers doublet. The magnetic field dependence involves both the Zeeman terms and the orbital vector potential terms, a fact that is responsible for the main difference between in-plane and out-of-plane magnetic fields with regard to qubit dynamics: the make up of the ground and first excited states is very different when the magnetic field is in the plane and when it is out of the plane.

For an out of plane magnetic field the hole g-factor is large, having a textbook value of 20.4 for Ge [20,114]. With the magnetic field out of the plane one can understand the physics qualitatively by considering an approximate decomposition of in-plane and out-of-plane dynamics by means of a Schrieffer-Wolff transformation [87]. The picture that emerges is that the top gate electric field primarily affects spin dynamics in the plane by enabling a Rashba term. In a quantum dot this Rashba term is responsible for a renormalization of the g-factor. In other words, one can think of the magnetic field terms as providing the qubit Zeeman splitting, and the Rashba spin-orbit terms as renormalizing this Zeeman splitting. Background charge fluctuations generating an electric field perpendicular to the plane are the biggest danger for this qubit, because they directly affect the Rashba interaction and through it the g-factor, generating pure dephasing. A more detailed analysis of hole spin qubit in $B_\perp$ [87] reveals that in-plane charge fluctuations do not produce pure dephasing to leading order. Hence for $B_\perp$ operation, when the qubit Zeeman splitting is at an extremum with respect to the top gate electric field [Fig. 6(b)], the qubit is protected against noise and one also observes a sweet spot in T_2^* in the vicinity of this point [Fig. 6(a)].

On the other hand, for hole spin qubit in $B_\parallel$, we recall that to a first approximation the in-plane g-factor is zero, hence the entire qubit Zeeman splitting is given by coupling to the excited states. This coupling involves Luttinger spin-orbit terms, the orbital magnetic field terms, the top gate electric field, and any other electric fields present in the system. The orbital terms due to the magnetic field mix the in-plane and out-of-plane coordinates regardless of the gauge choice. There is no clear separation between in-plane and out-of-plane dynamics, and no suitable Schrieffer-Wolff transformation from the 3D picture to the asymptotic 2D limit. One may at best envisage a combined Rashba-Zeeman interaction with contributions from all the components of the electric field, not just the top gate. The qubit states contain a strong admixture of all the higher orbital excited states in all three directions, which exposes the qubit to all components of the electric field of the defect. Thus, even though one can still identify an extremum in the qubit Zeeman splitting as a function of the top gate field [Fig. 5(b)], this does not offer full protection against noise [Fig. 5(a)]. It only protects against noise fields perpendicular to the plane, without offering any protection against the in-plane electric field of a defect. We check explicitly that for a defect that produces only an out-of-plane electric field at the qubit location the sensitivity to this out-of-plane noise is minim ized at the extremum in the Zeeman splitting. We have also checked that the qubit is not shielded from the in-plane electric field of the defect at this extremum: there is nothing special about the extremum from this perspective. We note that in an experimental sample exposed to an ensemble of defects it is possible for the net in-plane electric field to cancel out, or nearly cancel out. Hence, to achieve a more complete understanding of coherence, it is vital to consider a realistic configuration leading to $1/f$ noise. In light of this, and of additional complexities identified recently in modeling hole spin coherence [115], we defer the full theory of hole spin coherence in the presence of $1/f$ noise to a future publication.

We note that our findings appear to agree with recent experimental work reporting sweet spot operation of a Ge hole spin qubit [116] as well as strong anisotropy in the noise sensitivity. Sensitivity to charge noise is found to increase significantly when the qubit is operated in an in-plane magnetic field. This is in agreement with the finding of the present paper that in-plane magnetic fields expose the qubit to noise much more strongly than out-of-plane magnetic fields, leading to the coherence hot spot seen in Fig. 5(a). Remarkably, the dominant source of noise in Ref. [116] is believed to lie directly above the qubit, implying charge fluctuations predominantly in the perpendicular electric field component, and suggesting the qubit was not operated in the sweet spot for out-of-plane charge fluctuations. Nevertheless, a full comparison between theory and experiment is premature at this stage, given that tilting of the g-tensor and local strain have not been considered in the present work.

IV. ELLIPTICAL QUANTUM DOT

Introducing asymmetry into the planar confinement, i.e., having one lateral confinement potential stronger than the

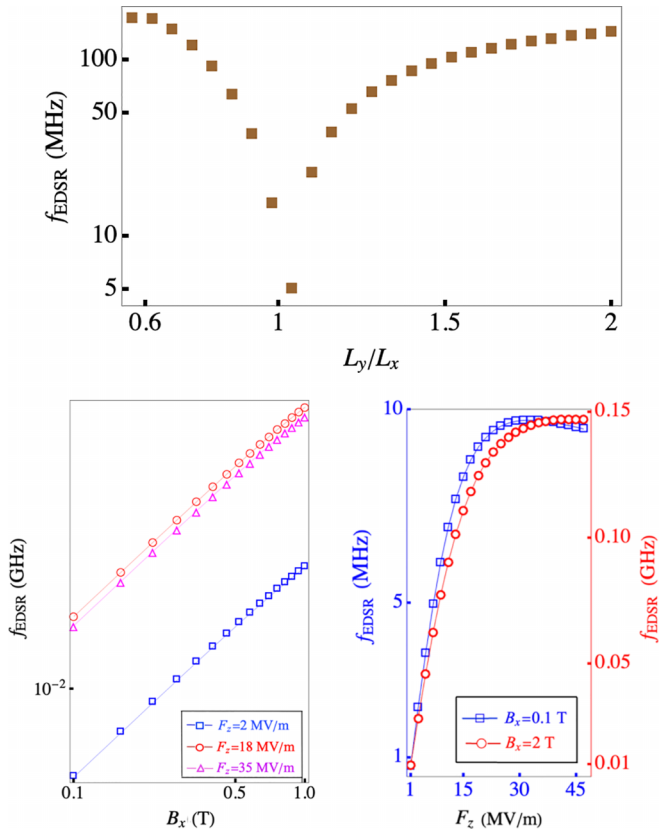

FIG. 7. (a)Variation of the EDSR Rabi frequency $f_{\rm EDSR}$ with the aspect ratio L_y/L_x of the hole QD. The confinement in x is fixed at $L_x = 50$nm while L_y is varied. The calculation is done for $B_x = 0.7$T. The EDSR driving field is applied along the $\hat{x}$ direction. $f_{\rm EDSR}$ is a minimum when the dot is circular, i.e., $L_x = L_y = 50$nm, while elliptical dots show an improvement of > 1 order of magnitude in the EDSR spin-flip rate at high ellipticities. (b) Linear monotonic dependence of $f_{\rm EDSR}$ on the applied in-plane magnetic field B_x for an elliptical dot with $L_y/L_x = 2$, $L_x = 50$nm for three different values of the top gate potential: $F_z = 2$, 18 , and 35 MV/m. (c) Variation in $f_{\rm EDSR}$ with the top gate electric field for an elliptical dot at low (0.1 T) and high (2 T) in-plane magnetic fields, displaying a maximum EDSR Rabi frequency at $F_z = 18$ and 21 MV/m, respectively.

other ($L_x \neq L_y$) will bring in additional sources of structure inversion asymmetry (SIA). For such elliptical hole QDs, the resultant Rashba spin-orbit interaction is stronger, bridging the gap between planar QD and nanowires [99] in terms of fast gate operations. A theoretical understanding of QD ellipticity for holes is thus important. Insight into our numerical results for elliptical hole QD (Fig. 7) can be obtained from the effective 2D spin-orbit Hamiltonian $H_{\rm SO}$ in Eq. (9) which contains the k^3-Rashba terms with spherical coefficient α_{R2} and cubic-symmetry coefficient α_{R3}:

$$\alpha_{R2} = \frac{3\hbar^4}{2m_0^2}\frac{\gamma_3\overline{\gamma}}{\Delta_{HL}}\langle\Psi_H|\Psi_L\rangle[\langle\Psi_H|\hat{k}_z|\Psi_L\rangle - \langle\Psi_L|\hat{k}_z|\Psi_H\rangle],$$

$$\alpha_{R3} = -\frac{3\hbar^4}{2m_0^2}\frac{\gamma_3\delta}{\Delta_{HL}}\langle\Psi_H|\Psi_L\rangle[\langle\Psi_H|\hat{k}_z|\Psi_L\rangle - \langle\Psi_L|\hat{k}_z|\Psi_H\rangle], \quad (12)$$

where $\overline{\gamma} = (\gamma_2 + \gamma_3)/2$, $\delta = (\gamma_2 - \gamma_3)/2$, with $\gamma_2 = 4.25$ and $\gamma_3 = 5.69$ being the Ge Luttinger parameters. Δ_{HL} signifies the HH-LH splitting, while, e.g., $\langle\Psi_H|\hat{k}_z|\Psi_L\rangle$, denote matrix elements between the HH and LH states. For the in-plane dimensions L_x, L_y of the hole quantum dot, the spherical term $\propto \alpha_{R2}$ scales as $\propto[1 - \frac{L_y^2}{L_x^2}]$ (Appendix B). Hence in a circular dot ($L_x = L_y$), only the cubic-symmetry correction α_{R3} is responsible for EDSR, while the α_{R2} term does not contribute to EDSR. In contrast, in an elliptical dot ($L_x \neq L_y$), the α_{R2} term makes a strong contribution to EDSR. Moreover, from Eq. (12) we can write $\alpha_{R3} = (\delta/\overline{\gamma})\,\alpha_{R2}$, which can be evaluated using Ge material parameters as $\alpha_2 \approx 10\,\alpha_3$ for elliptical dots (e.g., Table I). We present the results for a dot size of $L_z = 11$ nm, $L_x = 50$ nm, and varying L_y. Figure 7(a) shows the variation of the EDSR Rabi frequency with the aspect ratio L_x/L_y, showing that an increase in the aspect ratio results in a larger Rabi frequency. The qubit Zeeman splitting is linear in the applied in-plane magnetic field, similar to the circular case. The relaxation rate varies as B^3. The EDSR Rabi frequency is linear in B [Fig. 7(b)], which is reminiscent of out-of-plane B-field operation in presence of strong structure inversion asymmetry; and the Rabi frequency exhibits a maximum as a function of F_z [Fig. 7(c)].

V. *G*-FACTOR ANISOTROPY OF ELLIPTICAL QD AND COMPARISON WITH EXPERIMENT

The in-plane g-factor of an elliptical dot is strongly anisotropic and exhibits an oscillatory behavior as the magnetic field is rotated in the plane. We compare the predicted variation of the g-factor with experimentally measured values from EDSR in a planar germanium hole qubit. The qubit sample is a gate-defined double quantum dot in a $Ge/Si_{0.2}Ge_{0.8}$ heterostructure. (See Ref. [65] for further sample info). The dots are assumed to be elliptical, with a slight misalignment of their semimajor axes. Figure 8(a) shows a false color SEM of the gate design. Plunger gates (purple) are used to define the two dots, while the barrier gates (green) are used to control coupling to the leads and between the dots. Metal ohmic contacts (yellow) act as a reservoir for holes. By negatively biasing the barrier and plunger gates, the sample can be tuned to the few hole regime. The relative angle between the applied magnetic field direction in the plane and the double dot transport direction is denoted by θ. Bias triangles of the double dot measured via transport for positive and negative bias are shown in Figs. 8(b) and 8(c). A region of Pauli spin blockade is visible at the base of one charge transition as indicated by a yellow circle. By applying an external magnetic field and a microwave tone to the P2 gate, we are able to drive spin rotations via EDSR when the microwave frequency matches the Larmor frequency ($\hbar f = g\mu_B B$). These spin rotations lift the Pauli spin blockade, causing a change in the current through the double dot. Using a lock-in amplifier, we measure the difference in current through the double dot when the microwave is on versus off. Figure 8(d) shows the change in the leakage current for the double quantum dot with the external magnetic field applied in the direction indicated in Fig. 8(a). Clear EDSR lines are visible for both dots, and both single and multiphoton lines can be seen. From the slope of these

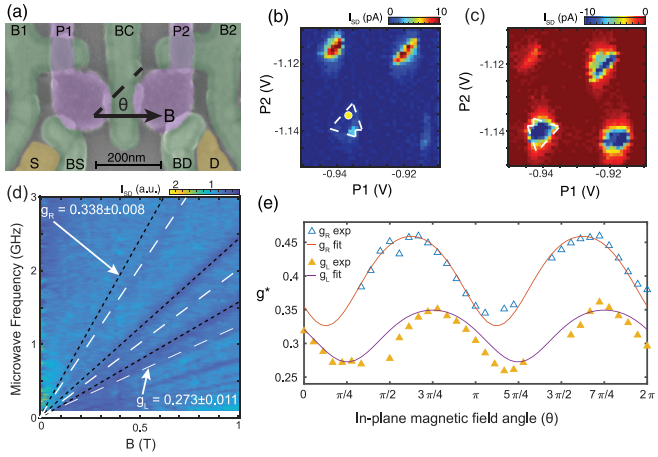

FIG. 8. (a) Sample scanning electron microscope (SEM) image of a gate-defined Ge double dot. [(b) and (c)] Bias triangles (dashed) in forward and reverse bias, respectively. Pauli spin blockade is visible in the transition marked by a yellow circle. (d) g-factors measured via EDSR for the magnetic field direction indicated in part (a) (black solid arrow). (e) Comparison of the g-factor measured via EDSR with the theoretical prediction. The experimental results for g-factor anisotropy in Ref. [117] are presented as scatter plots of effective g-factor (g^*) versus the in-plane magnetic field angular orientation with respect to the double dot transport direction (θ). We use triangular markers to denote the experimental data in scatter plots, while the solid fit lines are generated using the theoretical model in Sec. II. The g-factor for the left dot is denoted by g_L (empty blue triangular experimental data points, solid red theoretical fit line), while the right dot g-factor is denoted by g_R (filled yellow triangular experimental data points, solid purple theoretical fit line).

resonance lines the g-factor can be calculated for each dot. Using this technique, we measure the g-factor as a function of field angle by rotating a magnetic field of $B = 0.7$ T in the 2D plane. Figure 8(e) shows the results of this measurement for both quantum dots, revealing an oscillatory variation in the g-factor as a function of in-plane magnetic field angle. The direction of θ is shown in Fig. 8(a).

Using the model developed in Sec. II, we fit to the experimental data. For both dots, we use the same size, shape and strain. We are able to account for the difference in g-factor between the dots by considering only a rotation of the dot axes in-plane and a change in the magnitude of the vertical electric field. A full list of fitting parameters is given in Table II. The maximum value of the g-factor is not aligned with the external magnetic field or sample axes, and is also different for the left and right dots. To account for this, we introduce a phase shift angle (θ_{ps}) which effectively rotates the axes of the quantum dots. Here $\theta_{\mathrm{ps},l} = 3\pi/4$ and $\theta_{\mathrm{ps},r} = 5\pi/8$ The magnitude of the g-factor is also different for each dot. This is accounted for by changing the vertical electric field applied to each dot. Here we use 10MV/m for the left dot and 45MV/m for the right dot. The results of the fits for both dots are shown by the solid lines in Fig. 8(e).

The theoretical fit in Fig. 8(e) shows good agreement between the phase shift angle θ_{ps} parameter choices and B-field angular orientations where the experimental g-factors are maximum. In other words, the largest value of the g-factor occurs when the magnetic field is parallel to the semi-major axis of the elliptical hole QD. This behavior is consistent with the effective in-plane g-factor being primarily the result of coupling to higher excited states brought about by the orbital magnetic field terms. We note that inhomogeneous strain in the sample, or the Ge/SiGe heterostructure interface induced roughness and disorder, or a misalignment of the sample with respect to the in-plane B field (since $g_\perp \gg g_\parallel$) could potentially lead to significant modulation of the g-tensor. We can rule out the latter, since there is a different phase shift for the left and right dots in Fig. 8(e). The effects of strain and inhomogeneities on g-factor anisotropy will be considered in a future publication.

TABLE II. List of the parameters used to fit the analytical model to the experimental g-factor anisotropy data in Fig. 8(e). While the choices of phase shift angles (θ_{ps}) explain the experimental artifact of relative misalignment of the two dots; the top-gate voltages (F_z) are tuned to match the g-factor oscillation amplitudes of the dots. We stress however that the choice of fitting parameters given in this table for Fig. 8(e) is not unique. A possible set of parameters that yields a similar theoretical fitting of the experimental data in Fig. 8(e) are listed in Appendix E.

Fitting Parameters	values
Left QD in-plane dimensions	40 nm×30 nm
Right QD in-plane dimensions	40 nm×30 nm
Left dot perpendicular confinement ($L_{z,l}$)	10 nm
Right dot perpendicular confinement ($L_{z,r}$)	10 nm
Left dot top-gate voltage ($F_{z,l}$)	10 MV/m
Right dot top-gate voltage ($F_{z,r}$)	45 MV/m
Left dot phase shift $\theta_{\mathrm{ps},l}$	$3\pi/4$
Right dot phase shift $\theta_{\mathrm{ps},r}$	$5\pi/8$
Left dot uni-axial compressive strain $\varepsilon_{xx,l}$	−0.006
Right dot uni-axial compressive strain $\varepsilon_{xx,r}$	−0.006
Applied magnetic field magnitude B	0.7 T

VI. CONCLUSIONS AND OUTLOOK

We have presented a general ized model that fully describes the electrical operation of a planar germanium hole qubit in presence of an in-plane magnetic field. A comprehensive theory for spin manipulation via electron dipole spin resonance (EDSR) is given: surface inversion asymmetry (SIA) mediated fast EDSR is a result of the $\mathbf{k}\cdot\mathbf{p}$ coupling of the heavy hole ground state to higher energy light-hole bands. The EDSR rate is linear in B with important nonlinear corrections due to orbital mixing. Qubit relaxation is induced by acoustic phonons and the relaxation rate $1/T_1$ has terms with B^3, B^4, B^5 dependence, again reflecting the importance of the orbital mixing. In-plane operation demonstrates an excellent trade-off between relaxation and EDSR. The in-plane g-factor is strongly anisotropic and oscillates as the magnetic field is rotated in the plane. Random telegraph noise from charges in the plane of the quantum well results in decoherence, with an optimal top gate potential where it is insensitive to ΔF_z; although the in-plane magnetic field exposes the qubit to x-y electric field of the fluctuator. Hence, in contrast to the case of out-of-plane magnetic fields, coherence sweet spots cannot

be identified in an in-plane B for a qubit exposed to electric field fluctuations in all spatial directions. For an elliptical QD of aspect ratio $L_y/L_x = 2$, EDSR is shown to be faster by an order of magnitude compared to a circular dot of $L_x = 50$ nm radius; and the nonlinear correction to EDSR is suppressed as rotational asymmetry induces more SIA Rashba.

ACKNOWLEDGMENTS

This project is supported by the Australian Research Council Centre of Excellence in Future Low-Energy Electronics Technologies (Project No. CE170100039) and Discovery Project DP200100147. We acknowledge stimulating discussions with S. Das Sarma, M. Russ, X. Hu, and S. Liles.

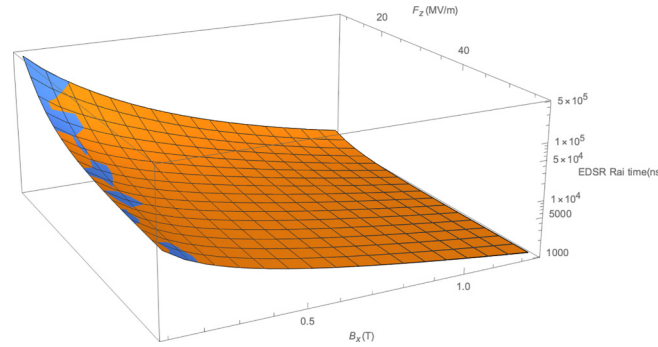

FIG. 9. EDSR time T_π (ns) vs top gate field F_z and in-plane magnetic field B_x.

APPENDIX A: GAUGE INVARIANCE

The hole motion in the topmost valence band is described by the 4×4 Luttinger-Kohn (LK) Hamiltonian, which in the general operator form is given by

$$H_{\rm LK} = \frac{\hbar^2}{2m_0}\left[\left(\gamma_1 + \frac{5\gamma_2}{2}\right)k^2 - 2\gamma_2\left(k_x^2J_x^2 + k_y^2J_y^2 + k_z^2J_z^2\right) - 4\gamma_3(\{k_x, k_y\}\{J_x, J_y\} + c.p.)\right] \tag{A1}$$

Expanding the anticommutators, LK Hamiltonian has the form:

$$H_{\rm LK} = \frac{\hbar^2}{2m_0}\left[\left(\gamma_1 + \frac{5\gamma_2}{2}\right)\left(k_x^2 + k_y^2 + k_z^2\right) - 2\gamma_2\left(k_x^2J_x^2 + k_y^2J_y^2 + k_z^2J_z^2\right) - 4\gamma_3\left(\left(\frac{k_xk_y + k_yk_x}{2}\right)\left(\frac{J_xJ_y + J_yJ_x}{2}\right)\right.\right.$$
$$\left.\left. + \left(\frac{k_yk_z + k_zk_y}{2}\right)\left(\frac{J_yJ_z + J_zJ_y}{2}\right) + \left(\frac{k_xk_z + k_zk_x}{2}\right)\left(\frac{J_xJ_z + J_zJ_x}{2}\right)\right)\right] \tag{A2}$$

with m_0 notifying bare electron mass, $\gamma_1 = 13.38$, $\gamma_2 = 4.24$, and $\gamma_3 = 5.69$ are Luttinger parameters. We have tried two different gauges: $\frac{1}{2}\mathbf{B}\times\mathbf{r}$ and gauge choice from Loss *et al.* [86].

1. Gauge 1

In presence of magnetic field, the momentum correction would be $\mathbf{k} \to (\mathbf{k} + \frac{e\mathbf{A}}{\hbar})$. We use the gauge $\mathbf{A} = -\frac{1}{2}B_zy\hat{\mathbf{e}}_\mathbf{x} + \frac{1}{2}B_zx\hat{\mathbf{e}}_\mathbf{y} + (B_xy - B_yx)\hat{\mathbf{e}}_\mathbf{z}$ (symmetric in z, Landau gauge in x-y).

a. Momentum correction.

(1) The components of corrected momentum:

$$k_x \to \left(k_x - \frac{eB_z}{2\hbar}y\right),\ k_y \to \left(k_y + \frac{eB_z}{2\hbar}x\right),\ k_z \to \left(k_z + \frac{eB_x}{\hbar}y - \frac{eB_y}{\hbar}x\right),$$

where $\mathbf{k} = -\iota\partial$. For $B_y = 0$ and $B_z = 0$, we write $k_x \to k_x$, $k_y \to k_y$, $k_z \to (k_z + \frac{eB_x}{\hbar}y)$.

(2) We evaluate k_i^2 terms below:

$$k_x^2 \Rightarrow k_x^2,\ k_y^2 \Rightarrow k_y^2,\ k_z^2 \Rightarrow \left(k_z^2 + \frac{2eB_xyk_z}{\hbar} + \frac{e^2B_x^2y^2}{\hbar^2}\right) \tag{A3}$$

and the cross-terms k_ik_j are

$$k_xk_y \Rightarrow k_xk_y;\ k_yk_z \Rightarrow \left(k_yk_z + \frac{eB_x}{\hbar}\{y, k_y\}\right);\ k_xk_z \Rightarrow \left(k_xk_z + \frac{eB_xyk_x}{\hbar}\right). \tag{A4}$$

(3) Using these corrections, the LK Hamiltonian is

$$H_{\rm LK} = \left[\left(\gamma_1 + \frac{5\gamma_2}{2}\right)\left(k_x^2 + k_y^2 + k_z^2 + \frac{2eB_xyk_z}{\hbar} + \frac{e^2B_x^2y^2}{\hbar^2}\right) - 2\gamma_2\left(k_x^2J_x^2 + k_y^2J_y^2 + \left(k_z^2 + \frac{2eB_xyk_z}{\hbar} + \frac{e^2B_x^2y^2}{\hbar^2}\right)J_z^2\right)\right.$$
$$\left. - 4\gamma_3\left(k_xk_y\{J_x, J_y\} + \left(k_yk_z + \frac{eB_x}{\hbar}\{y, k_y\}\right)\{J_y, J_z\} + \left(k_xk_z + \frac{eB_xyk_x}{\hbar}\right)\{J_z, J_x\}\right)\right]\frac{\hbar^2}{2m_0}, \tag{A5}$$

where

$$H_{\rm LK}^{11/22} = \frac{\hbar^2}{2m_0}\Big[(\gamma_1 - 2\gamma_2)\Big(k_z^2 + \frac{2eB_x y k_z}{\hbar} + \frac{e^2B_x^2y^2}{\hbar^2}\Big) + (\gamma_1 + \gamma_2)\big(k_x^2 + k_y^2\big)\Big],$$
$$H_{\rm LK}^{33/44} = \frac{\hbar^2}{2m_0}\Big[(\gamma_1 + 2\gamma_2)\Big(k_z^2 + \frac{2eB_x y k_z}{\hbar} + \frac{e^2B_x^2y^2}{\hbar^2}\Big) + (\gamma_1 - \gamma_2)\big(k_x^2 + k_y^2\big)\Big],$$
$$H_{\rm LK}^{13} = L = -\sqrt{3}\frac{\hbar^2\gamma_3}{m_0}\Big[\Big(k_x k_z + \frac{eB_x y k_x}{\hbar}\Big) - i\Big(k_y k_z + \frac{eB_x}{\hbar}\{y, k_y\}\Big)\Big],$$
$$H_{\rm LK}^{14} = M = \frac{\sqrt{3}\hbar^2}{2m_0}\big[-\gamma_2\big(k_x^2 - k_y^2\big) + 2i\gamma_3 k_x k_y\big]. \tag{A6}$$

2. Gauge 2

In this section, we use the symmetric gauge ($\frac{1}{2}\mathbf{B}\times\mathbf{r}$): $\mathbf{A} = \frac{1}{2}(B_y z - B_z y)\hat{\mathbf{e}}_\mathbf{x} + \frac{1}{2}(B_z x - B_x z)\hat{\mathbf{e}}_\mathbf{y} + \frac{1}{2}(B_x y - B_y x)\hat{\mathbf{e}}_\mathbf{z}$.

b. Momentum correction.

(1) The components of corrected momentum with $B_y = 0, B_z = 0$:

$$k_x \to k_x,\ k_y \to \Big(k_y - \frac{eB_x}{2\hbar}z\Big),\ k_z \to \Big(k_z + \frac{eB_x}{2\hbar}y\Big) \text{ where, } \mathbf{k} = -\iota\partial. \tag{A7}$$

(2) We evaluate k_i^2 terms below:

$$k_x^2 \Rightarrow k_x^2,\ k_y^2 \Rightarrow \Big(k_y^2 - \frac{eB_x z k_y}{\hbar} + \frac{e^2B_x^2z^2}{4\hbar^2}\Big),\ k_z^2 \Rightarrow \Big(k_z^2 + \frac{eB_x y k_z}{\hbar} + \frac{e^2B_x^2y^2}{4\hbar^2}\Big) \tag{A8}$$

and the cross-terms $k_i k_j$ are

$$k_x k_y \Rightarrow \Big(k_x k_y - \frac{eB_x z k_x}{2\hbar}\Big); k_y k_z \Rightarrow \Big(k_y k_z + \frac{eB_x}{2\hbar}(\{y, k_y\} - \{z, k_z\}) - \frac{e^2B_x^2}{4\hbar^2}yz\Big); k_x k_z \Rightarrow \Big(k_x k_z + \frac{eB_x y k_x}{2\hbar}\Big). \tag{A9}$$

(3) Using these corrections, the LK Hamiltonian terms become

$$H_{\rm LK} = \frac{\hbar^2}{2m_0}\Big[\Big(\gamma_1 + \frac{5\gamma_2}{2}\Big)\Big(k_x^2 + k_y^2 - \frac{eB_x z k_y}{\hbar} + \frac{e^2B_x^2z^2}{4\hbar^2} + k_z^2 + \frac{eB_x y k_z}{\hbar} + \frac{e^2B_x^2y^2}{4\hbar^2}\Big)$$
$$- 2\gamma_2\Big(k_x^2J_x^2 + \Big(k_y^2 - \frac{eB_x z k_y}{\hbar} + \frac{e^2B_x^2z^2}{4\hbar^2}\Big)J_y^2 + \Big(k_z^2 + \frac{eB_x y k_z}{\hbar} + \frac{e^2B_x^2y^2}{4\hbar^2}\Big)J_z^2\Big) - 4\gamma_3\Big(\Big(k_x k_y - \frac{eB_x z k_x}{2\hbar}\Big)\{J_x, J_y\}$$
$$+\Big(k_y k_z + \frac{eB_x}{2\hbar}\{y, k_y\} - \frac{eB_x}{2\hbar}\{z, k_z\} - \frac{e^2B_x^2}{4\hbar^2}yz\Big)\{J_y, J_z\} + \Big(k_x k_z + \frac{eB_x y k_x}{2\hbar}\Big)\{J_z, J_x\}\Big)\Big], \tag{A10}$$

where

$$H_{\rm LK}^{11/22} = \frac{\hbar^2}{2m_0}\Big[(\gamma_1 - 2\gamma_2)\Big(k_z^2 + \frac{2eB_x y k_z}{\hbar} + \frac{e^2B_x^2y^2}{\hbar^2}\Big) + (\gamma_1 + \gamma_2)\Big(k_x^2 + k_y^2 - \frac{eB_x z k_y}{\hbar} + \frac{e^2B_x^2z^2}{4\hbar^2}\Big)\Big], \tag{A11}$$
$$H_{\rm LK}^{33/44} = \frac{\hbar^2}{2m_0}\Big[(\gamma_1 + 2\gamma_2)\Big(k_z^2 + \frac{2eB_x y k_z}{\hbar} + \frac{e^2B_x^2y^2}{\hbar^2}\Big) + (\gamma_1 - \gamma_2)\Big(k_x^2 + k_y^2 - \frac{eB_x z k_y}{\hbar} + \frac{e^2B_x^2z^2}{4\hbar^2}\Big)\Big], \tag{A12}$$
$$H_{\rm LK}^{13} = L = -\sqrt{3}\frac{\hbar^2\gamma_3}{m_0}\Big[\Big(k_x k_z + \frac{eB_x y k_x}{2\hbar}\Big) - i\Big(k_y k_z + \frac{eB_x}{2\hbar}\{y, k_y\} - \frac{eB_x}{2\hbar}\{z, k_z\} - \frac{e^2B_x^2}{4\hbar^2}yz\Big)\Big],$$
$$H_{\rm LK}^{14} = M = \frac{\sqrt{3}\hbar^2}{2m_0}\Big[-\gamma_2\Big(k_x^2 - k_y^2 + \frac{eB_x z k_y}{\hbar} - \frac{e^2B_x^2z^2}{4\hbar^2}\Big) + 2i\gamma_3\Big(k_x k_y - \frac{eB_x z k_x}{2\hbar}\Big)\Big]. \tag{A13}$$

Figure 9 shows the variation of the EDSR Rabi frequency $f_{\rm EDSR}$ with respect to the applied magnetic field strength B_x and top-gate field strength F_z for both gauge choices; emphasising the gauge invariance of the model.

APPENDIX B: SCHRIEFFER-WOLFF TRANSFORMATION

A Hamiltonian $H = H^0 + H'$ comprising two parts: H^0 with known eigenvalues E_n and eigenfunctions $|\Psi_n\rangle$, and a perturbation H'; can be treated in quasidegenerate perturbation theory which is particularly suitable for approximate diagonalization of $\mathbf{k}\cdot\mathbf{p}$ subband Hamiltonians. The set of eigenfunctions $\{|\Psi_n\rangle\}$ can be divided in subsets A and B, which are weakly interacting via perturbation. The quasidegenerate perturbation theory produces a unitary transformation $\tilde{H} = e^{-S}He^{S}$, such that the matrix

elements of $\tilde{H}$ between eigenfunctions $|\Psi_l\rangle$ from set A and $|\Psi_m\rangle$ from set B vanishes: $\langle\Psi_n|\tilde{H}|\Psi_l\rangle = 0$. In the context of this work, this unitary transformation is known as Schrieffer-Wolff transformation. S can be calculated using the anti-Hermiticity property $S^\dagger = -S$, which allows one to evaluate the transformed Hamiltonian as $\tilde{H} = H^{(0)} + H^{(1)} + H^{(2)} + H^{(3)} + \ldots$ The expansion signifies the diagonalization of the subband Hamiltonian in increasing order of subband interactions:

$$
\begin{aligned}
H^{(0)}_{mm'} &= H^0_{mm'},\\
H^{(1)}_{mm'} &= H'_{mm'},\\
H^{(2)}_{mm'} &= \frac{1}{2}\sum_l H'_{ml}H'_{lm'}\left[\frac{1}{E_m - E_l} + \frac{1}{E_{m'} - E_l}\right],\\
H^{(3)}_{mm'} &= -\frac{1}{2}\sum_{l,m''}\left[\frac{H'_{ml}H'_{lm''}H'_{m''m'}}{(E_{m'} - E_l)(E_{m''} - E_l))} + \frac{H'_{mm''}H'_{m''l}H'_{lm'}}{(E_m - E_l)(E_{m''} - E_l))}\right]\\
&\quad + \frac{1}{2}\sum_{l,l'} H'_{ml}H'_{ll'}H'_{l'm'}\left[\frac{1}{(E_m - E_l)(E_m - E_{l'})} + \frac{1}{(E_{m'} - E_l)(E_{m'} - E_{l'})}\right],
\end{aligned}
\tag{B1}
$$

where $m,\ m',\ m''$ denotes states from set A and $l,\ l',\ l''$ denotes higher energy states from set B.

1. 3D Hamiltonian to effective 2D Hamiltonian

Applying Eq. (B1) to the 4×4 quantum dot Hamiltonian with large HH-LH splitting in the $j = |\frac{3}{2}\rangle$ basis, we derive the final formula in Eq. (7) for writing down the effective 2×2 transformed Hamiltonian in the lowest energy HH states. We derive the matrix elements of the 2×2 Hamiltonian explicitly here. Not including the uni-axial strain terms, first we identify H^0 and H' from Eq. (1) as follows:

$$
H^0 = \left(\begin{array}{cc|cc} P+Q & 0 & 0 & 0\\ 0 & P+Q & 0 & 0\\ \hline 0 & 0 & P-Q & 0\\ 0 & 0 & 0 & P-Q \end{array}\right);\ H' = \left(\begin{array}{cc|cc} 0 & 0 & L & M\\ 0 & 0 & M^* & -L^*\\ \hline L^* & M & 0 & 0\\ M^* & -L & 0 & 0 \end{array}\right),
\tag{B2}
$$

where the Luttinger Hamltonian has the following matrix elements: $P+Q = \frac{\hbar^2}{2m_0}(\gamma_1 - 2\gamma_2)k_z^2 + \frac{\hbar^2}{2m_0}(\gamma_1 + \gamma_2)k_\parallel^2$, with $k_\parallel^2 = k_x^2 + k_y^2$, $L = \frac{-\sqrt{3}\hbar^2\gamma_3}{m_0}k_- k_z$ and $M = -\frac{\sqrt{3}\hbar^2}{2m_0}(-\overline{\gamma}k_-^2 + \delta k_+^2)$. $k_\pm = k_x \pm ik_y$, $\overline{\gamma} = \frac{\gamma_2+\gamma_3}{2}$, $\delta = \frac{\gamma_2-\gamma_3}{2}$ are defined. One can readily calculate $H^{(0)} = \left(\begin{smallmatrix} P+Q & 0\\ 0 & P+Q\end{smallmatrix}\right)$, $H^{(1)} = \left(\begin{smallmatrix} 0 & 0\\ 0 & 0\end{smallmatrix}\right)$. In the second order of Schrieffer-Wolff transformation, the diagonal terms would be

$$
\begin{aligned}
H^{(2)}_{11} &= \frac{1}{2}\sum_{l=3,4} H'_{1l}H'_{l1}\left[\frac{1}{E_1 - E_l} + \frac{1}{E_1 - E_l}\right] = H'_{13}H'_{31}\left[\frac{1}{E_1 - E_3}\right] + H'_{14}H'_{41}\left[\frac{1}{E_1 - E_4}\right]\\
&= -\frac{\langle L\rangle_{HL}\langle L^*\rangle_{LH}}{\Delta_{HL}} - \frac{\langle M\rangle_{HL}\langle M^*\rangle_{LH}}{\Delta_{HL}}\\
&= -\frac{1}{\Delta_{HL}}\left[\left(\frac{\sqrt{3}\hbar^2\gamma_3}{m_0}\right)^2 k_-k_+\langle H|\hat{k}_z|L\rangle\langle L|\hat{k}_z|H\rangle + \left(-\frac{\sqrt{3}\hbar^2}{2m_0}\right)^2(\overline{\gamma}k_-^2 + \delta k_+^2)(\overline{\gamma}k_+^2 + \delta k_-^2)\langle H|L\rangle\langle L|H\rangle\right]\\
&= -\frac{1}{\Delta_{HL}}\left[\left(\frac{\sqrt{3}\hbar^2\gamma_3|\langle H|\hat{k}_z|L\rangle|}{m_0}\right)^2\left(k_x^2 + k_y^2\right) + \left(\frac{\sqrt{3}\hbar^2|\langle H|L\rangle|}{2m_0}\right)^2\left((\overline{\gamma}^2 + \delta^2)k_-^2k_+^2 + \overline{\gamma}\delta(k_-^4 + k_+^4)\right)\right]\\
&= -\frac{1}{\Delta_{HL}}\left[\left(\frac{\sqrt{3}\hbar^2\gamma_3|\langle H|\hat{k}_z|L\rangle|}{m_0}\right)^2\left(k_x^2 + k_y^2\right) + \left(\frac{\sqrt{3}\hbar^2|\langle H|L\rangle|}{2m_0}\right)^2\left((\overline{\gamma}^2 + \delta^2)\left(k_x^2 + k_y^2\right)^2 + \overline{\gamma}\delta((k_+^2 - k_-^2)^2 + 2k_+^2k_-^2)\right)\right]\\
&= -\frac{1}{\Delta_{HL}}\left[\left(\frac{\sqrt{3}\hbar^2\gamma_3|\langle H|\hat{k}_z|L\rangle|}{m_0}\right)^2\left(k_x^2 + k_y^2\right) + \left(\frac{\sqrt{3}\hbar^2|\langle H|L\rangle|}{2m_0}\right)^2\left(\gamma_2^2\left(k_x^2 + k_y^2\right)^2 + \frac{1}{4}\left(\gamma_2^2 - \gamma_3^2\right)(k_+^2 - k_-^2)^2\right)\right]\\
&= -\frac{1}{\Delta_{HL}}\left[\left(\frac{\sqrt{3}\hbar^2\gamma_3|\langle H|\hat{k}_z|L\rangle|}{m_0}\right)^2 k_\parallel^2 + \left(\frac{\sqrt{3}\hbar^2|\langle H|L\rangle|}{2m_0}\right)^2\left(\gamma_2^2k_\parallel^4 + \frac{1}{4}\left(\gamma_2^2 - \gamma_3^2\right)(k_+^2 - k_-^2)^2\right)\right].
\end{aligned}
\tag{B3}
$$

So up to second order in SW transformation, $H_{\rm eff}^{11} = \tilde{H}_{11}$ can be written as

$$H_{\rm eff}^{11} = \frac{\hbar^2}{2m_0}(\gamma_1 - 2\gamma_2)\langle H|\hat{k_z^2}|L\rangle + \frac{\hbar^2}{2m_0}(\gamma_1+\gamma_2)k_\parallel^2 - \frac{1}{\Delta_{HL}}\left[\left(\frac{\sqrt{3}\hbar^2\gamma_3|\langle H|\hat{k}_z|L\rangle|}{m_0}\right)^2 k_\parallel^2 + \left(\frac{\sqrt{3}\hbar^2|\langle H|L\rangle|}{2m_0}\right)^2\left(\gamma_2^2 k_\parallel^4 + \frac{1}{4}\left(\gamma_2^2-\gamma_3^2\right)(k_+^2-k_-^2)^2\right)\right]. \tag{B4}$$

The first term $\propto \langle H|\hat{k_z^2}|L\rangle$ does not contribute to in-plane hole dynamics and only renormalizes the z-subband energies; hence safely discarded subsequently. Noting the degeneracy of the diagonal elements, one can similarly calculate $H_{\rm eff}^{22}$; resulting in the diagonal hole kinetic energy term H_0 in Eq. (9) as follows:

$$H_0 = \left[\left(\frac{\hbar^2}{2m_0}(\gamma_1+\gamma_2) - \frac{3\hbar^4\gamma_3^2|\langle H|\hat{k}_z|L\rangle|^2}{m_0^2\Delta_{HL}}\right)k_\parallel^2 - \frac{3\hbar^4\gamma_2^2|\langle H|L\rangle|^2}{4m_0^2\Delta_{HL}}k_\parallel^4 - \frac{3\hbar^4\left(\gamma_2^2-\gamma_3^2\right)|\langle H|L\rangle|^2}{16m_0^2\Delta_{HL}}(k_+^2-k_-^2)^2\right]I_{2\times2}. \tag{B5}$$

The off-diagonal spin-orbit terms are calculated in second order of SW as follows:

$$\begin{aligned}
H_{12}^{(2)} &= \frac{1}{2}\sum_{l=3,4} H'_{1l}H'_{l2}\left[\frac{1}{E_1-E_l}+\frac{1}{E_2-E_l}\right] \\
&= \frac{1}{2}H'_{13}H'_{32}\left[\frac{1}{E_1-E_3}+\frac{1}{E_2-E_3}\right] + \frac{1}{2}H'_{14}H'_{42}\left[\frac{1}{E_1-E_4}+\frac{1}{E_2-E_4}\right] \\
&= -\frac{\langle L\rangle_{HL}\langle M\rangle_{LH}}{\Delta_{HL}} + \frac{\langle M\rangle_{HL}\langle L\rangle_{LH}}{\Delta_{HL}} \\
&= \frac{1}{\Delta_{HL}}\left[\left(\frac{3\hbar^4\gamma_3}{2m_0^2}\right)(\overline{\gamma}k_-^2+\delta k_+^2)\langle H|L\rangle k_-\langle L|\hat{k}_z|H\rangle - \left(\frac{3\hbar^4\gamma_3}{2m_0^2}\right)k_-\langle H|\hat{k}_z|L\rangle(\overline{\gamma}k_-^2+\delta k_+^2)\langle L|H\rangle\right] \\
&= \frac{3\hbar^4\gamma_3}{2m_0^2\Delta_{HL}}\left[(\overline{\gamma}k_-^2+\delta k_+^2)\langle H|L\rangle k_-\langle L|\hat{k}_z|H\rangle - k_-\langle H|\hat{k}_z|L\rangle(\overline{\gamma}k_-^2+\delta k_+^2)\langle L|H\rangle\right] \\
&= \frac{3\hbar^4\gamma_3\overline{\gamma}}{2m_0^2\Delta_{HL}}\left[k_-^3\langle H|L\rangle\left(\langle L|\hat{k}_z|H\rangle - \langle H|\hat{k}_z|L\rangle\right)\right] + \frac{3\hbar^4\gamma_3\delta}{2m_0^2\Delta_{HL}}[\{k_+^2,k_-\}\langle H|L\rangle\left(\langle L|\hat{k}_z|H\rangle - \langle H|\hat{k}_z|L\rangle\right)];
\end{aligned} \tag{B6}$$

similarly,

$$H_{21}^{(2)} = \frac{3\hbar^4\gamma_3\overline{\gamma}}{2m_0^2\Delta_{HL}}[k_+^3\langle H|L\rangle\left(\langle L|\hat{k}_z|H\rangle - \langle H|\hat{k}_z|L\rangle\right)] + \frac{3\hbar^4\gamma_3\delta}{2m_0^2\Delta_{HL}}[\{k_-^2,k_+\}\langle H|L\rangle\left(\langle L|\hat{k}_z|H\rangle - \langle H|\hat{k}_z|L\rangle\right)]. \tag{B7}$$

This produces the spin-orbit 2D Hamiltonian:

$$H_{\rm SO} = \frac{3\hbar^4\gamma_3}{2m_0^2\Delta_{HL}}(\langle H|\hat{k}_z|L\rangle - \langle L|\hat{k}_z|H\rangle)[\overline{\gamma}(k_+^3\sigma_- - k_-^3\sigma_+) - \delta(\{k_+^2,k_-\})\sigma_+ - \{k_+,k_-^2\})\sigma_-]. \tag{B8}$$

Next we analyze the Zeeman spin-splitting terms in the 2D approximation. Firstly, we write the angular momentum matrices in $j = 3/2$ basis:

$$J_x = \frac{1}{2}\begin{pmatrix} 0 & 0 & \sqrt{3} & 0 \\ 0 & 0 & 0 & \sqrt{3} \\ \sqrt{3} & 0 & 0 & 2 \\ 0 & \sqrt{3} & 2 & 0 \end{pmatrix};\ J_y = \frac{i}{2}\begin{pmatrix} 0 & 0 & -\sqrt{3} & 0 \\ 0 & 0 & 0 & \sqrt{3} \\ \sqrt{3} & 0 & 0 & -2 \\ 0 & -\sqrt{3} & 2 & 0 \end{pmatrix};\ J_z = \frac{1}{2}\begin{pmatrix} 3 & 0 & 0 & 0 \\ 0 & -3 & 0 & 0 \\ 0 & 0 & 1 & 0 \\ 0 & 0 & 0 & -1 \end{pmatrix}. \tag{B9}$$

An external in-plane magnetic field B_x gives rise to the Zeeman interaction $H_Z = (-2\kappa\mu_B B_x J_x - 2q\mu_B B_x J_x^3)$ in the 3D model:

$$H_Z = \begin{pmatrix} 0 & \frac{3}{2}q\mu_B B_x & \left(\frac{7q}{4}+\kappa\right)\sqrt{3}\mu_B B_x & 0 \\ \frac{3}{2}q\mu_B B_x & 0 & 0 & \left(\frac{7q}{4}+\kappa\right)\sqrt{3}\mu_B B_x \\ \left(\frac{7q}{4}+\kappa\right)\sqrt{3}\mu_B B_x & 0 & 0 & (5q+2\kappa)\mu_B B_x \\ 0 & \left(\frac{7q}{4}+\kappa\right)\sqrt{3}\mu_B B_x & (5q+2\kappa)\mu_B B_x & 0 \end{pmatrix}. \tag{B10}$$

The bare Zeeman terms in the 2D model up to third order can be calculated from Schrieffer-Wolff transformation: $H_{Z,2D}^{(0)} = \left(\begin{smallmatrix} 0 & 0 \\ 0 & 0 \end{smallmatrix}\right)$, $H_{Z,2D}^{(1)} = \left(\begin{smallmatrix} 0 & \frac{3}{2}q\mu_B B_x \\ \frac{3}{2}q\mu_B B_x & 0 \end{smallmatrix}\right)$, $H_{Z,2D}^{(2)} = \left(\begin{smallmatrix} 0 & 0 \\ 0 & 0 \end{smallmatrix}\right)$, $H_{Z,2D}^{(3)} = \left(\begin{smallmatrix} 0 & g_1\mu_B^3 B_x^3 \\ g_1\mu_B^3 B_x^3 & 0 \end{smallmatrix}\right)$. We calculate $g_1 = 3(\frac{7q}{4}+\kappa)^2(2\kappa+\frac{17}{4}q)/\Delta_{HL}^2 \approx$

$\frac{6\kappa^3}{\Delta_{HL}^2}$. We mention here that the correction in diagonal terms in higher order of perturbation due to B_x only renormalizes the z subbands and does not contribute to a Zeeman splitting, hence not shown explicitly above. Considering canonical momentum in the symmetric gauge: $\mathbf{k} = \{k_x, k_y - \frac{eB_x}{2\hbar}z, k_z + \frac{eB_x}{2\hbar}y\}$ in presence of the external magnetic field, we get a correction in $H_{\mathbf{eff}}^{2\times2}$ off-diagonal which is proportional to $B_x k_x^2$, because the $\langle L\rangle_{HL}\langle M\rangle_{LH}$ etc. terms in set of equations (B6) gets modified as follows:

$$\langle L\rangle_{HL}\langle M\rangle_{LH} = \left[k_-\langle k_z\rangle_{HL} + \frac{ieB_x}{2\hbar}\langle\{z, k_z\}\rangle_{HL}\right]\left[(\overline{\gamma}k_-^2 + \delta k_+^2)\langle L|H\rangle + \frac{ieB_x\langle z\rangle_{LH}}{\hbar}(\overline{\gamma}k_- - \delta k_+)\right]. \tag{B11}$$

This gives rise to terms e.g. $g_2\mu_B B_x k_x^2\sigma_x$ in $H_{Z,2D}$, where g_2 can be estimated as

$$g_2 \simeq \frac{3\hbar^4\gamma_3}{2\Delta_{HL}m_0^2\mu_B}\frac{ie}{\hbar}[\gamma_2\langle H|L\rangle(\langle L\{\hat{z}, \hat{k_z}\}|H\rangle - \langle H\{\hat{z}, \hat{k_z}\}|L\rangle) + 2\gamma_3(\langle H|\hat{z}|L\rangle\langle L|\hat{k_z}|H\rangle - \langle L|\hat{z}|H\rangle\langle H|\hat{k_z}|L\rangle)]. \tag{B12}$$

For a typical hole number density of $p = 2\times10^{15}$ m^{-2}, which correspond to a top-gate potential of $F_z \approx 2.5$ MV/m ($F_z \approx \frac{ep}{(16.2-4.5x)\epsilon_0}$, $x = 0.2$ in Si_xGe_{1-x}), we calculate the 2D model parameters from our knowledge of the z-subband interactions, as outlined in this section. Values for these parameters are provided in the main text Table I.

2. effective 2D Hamiltonian to two level EDSR Hamiltonian

To evaluate the B_x dependence of f_{EDSR} in the effective 2D model, we project $H_{\mathrm{eff}}^{2\times2}$ into the following in-plane states:

$$\left\{\frac{e^{-\left(\frac{x^2}{2L_x^2}+\frac{y^2}{2L_y^2}\right)}}{\sqrt{\pi L_x L_y}}, \frac{\sqrt{2}y\, e^{-\left(\frac{x^2}{2L_x^2}+\frac{y^2}{2L_y^2}\right)}}{\sqrt{\pi L_y^3 L_x}}, \frac{\sqrt{2}x\, e^{-\left(\frac{x^2}{2L_x^2}+\frac{y^2}{2L_y^2}\right)}}{\sqrt{\pi L_x^3 L_y}}\right\}\otimes\{\uparrow, \downarrow\}, \tag{B13}$$

where the orbital states are the first three harmonic oscillator product states: $(n, m) = \{(0, 0), (0, 1), (1, 0)\}$. Considering the general case of $L_x \neq L_y$, we denote the orbital energies of these states as E_0, E_1, E_2. The spinors are the effective spin-up and spin-down states of the 2D hole qubit, and gives $\pm g_\parallel\mu_B B_x$ Zeeman energies for the up and down spin states due to small anisotropic term q and the orbital $\mathbf{B}$ terms $\propto B_x k_x^2$. The spin-orbit interactions can be listed as

$$H_{\mathrm{SO}} = i\alpha_{R1}(k_-\sigma_- - k_+\sigma_+) + i\alpha_{R2}(k_+^3\sigma_- - k_-^3\sigma_+) + i\alpha_{R3}(\{k_+, k_-^2\}\sigma_- - \{k_+^2, k_-\}\sigma_+) + i\alpha_{R4}\left(\left\{k_z^2, k_-\right\}\sigma_- - \left\{k_z^2, k_+\right\}\sigma_+\right). \tag{B14}$$

The k-linear Rashba terms come from the coupling of the bonding VB p orbitals to the antibonding CB p orbitals, which is very small. In the Luttinger formalism, thus the α_{R1}, α_{R4} terms vanish. The nonzero contributions are

$$H_{\mathrm{SO}} = i\alpha_{R2}(k_+^3\sigma_- - k_-^3\sigma_+) + i\alpha_{R3}(\{k_+, k_-^2\}\sigma_- - \{k_+^2, k_-\}\sigma_+) \tag{B15}$$

and the spin-orbit matrix elements are calculated below:

$$\begin{aligned}
\langle(0,0)\uparrow|H_{\mathrm{SO}}|(0,1)\downarrow\rangle &= -i\alpha_{R2}\langle(0,0)\uparrow|k_-^3\sigma_+|(0,1)\downarrow\rangle + i\alpha_{R3}\langle(0,0)\uparrow|k_+k_-k_+\sigma_+|(0,1)\downarrow\rangle \\
&= -i\alpha_{R2}\langle(0,0)|k_-^3|(0,1)\rangle + i\alpha_{R3}\langle(0,0)|k_+k_-k_+|(0,1)\rangle \\
&= \frac{-3i\alpha_{R2}}{2\sqrt{2}L_y^3}\left(1 - \frac{L_y^2}{L_x^2}\right) + \frac{i\alpha_{R3}}{2\sqrt{2}L_y^3}\left(1 + 3\frac{L_y^2}{L_x^2}\right) = R_c, \qquad \text{(B16)} \\
\langle(0,0)\uparrow|H_{\mathrm{SO}}|(1,0)\downarrow\rangle &= -i\alpha_{R2}\langle(0,0)\uparrow|k_-^3\sigma_+|(1,0)\downarrow\rangle + i\alpha_{R3}\langle(0,0)\uparrow|k_+k_-k_+\sigma_+|(1,0)\downarrow\rangle \\
&= -i\alpha_{R2}\langle(0,0)|k_-^3|(0,1)\rangle + i\alpha_{R3}\langle(0,0)|k_+k_-k_+|(0,1)\rangle \\
&= \frac{-3\alpha_{R2}}{2\sqrt{2}L_xL_y^2}\left(1 - \frac{L_y^2}{L_x^2}\right) + \frac{\alpha_{R3}}{2\sqrt{2}L_xL_y^2}\left(1 + 3\frac{L_y^2}{L_x^2}\right) = R_r. \qquad \text{(B17)}
\end{aligned}$$

The ac electric field $eE_x(t)x$ is spin-conserving and connects the states (0,0) and (1,0). In other words, the driving electric field generates $\Delta n = 1$ orbital transition. On the other hand, the spin-orbit coupling H_{SO} connects $(0, 0, \uparrow)$ and $(1, 0, \downarrow)$, i.e., also generates $\Delta n = 1$ orbital transition but along with a spin-flip. $eE_x(t)x + H_{\mathrm{SO}}$ thus effectively results in a spin-flip, known as electrically driven spin resonance (EDSR). Hence, to effectively describe hole EDSR in the effective 2D model, one need to capture all spin interactions and $\Delta n = 1$ orbital transitions up to the lowest order; which is possible by choosing a basis

consisting of the ground orbital state and first excited orbital states. The resultant 6×6 Hamiltonian would be

$$H' = \begin{pmatrix} E_0 - \frac{1}{2}g_\parallel \mu_B B_x & 0 & 0 & R_c & eE_x a & R_r \\ 0 & E_0 + \frac{1}{2}g_\parallel \mu_B B_x & R_c^* & 0 & -R_r & eE_x a \\ 0 & R_c & E_1 - \frac{1}{2}g_\parallel \mu_B B_x & 0 & 0 & 0 \\ R_c^* & 0 & 0 & E_1 + \frac{1}{2}g_\parallel \mu_B B_x & 0 & 0 \\ eE_x a & -R_r & 0 & 0 & E_2 - \frac{1}{2}g_\parallel \mu_B B_x & 0 \\ R_r & eE_x a & 0 & 0 & 0 & E_2 + \frac{1}{2}g_\parallel \mu_B B_x \end{pmatrix}. \tag{B18}$$

Second-order perturbation theory gives the EDSR matrix element as

$$\begin{aligned} \tilde{H}_{12} &= \sum_{j=3}^{6} \frac{1}{2} H'_{1j} H'_{j2} \left(\frac{1}{\epsilon_1 - \epsilon_j} + \frac{1}{\epsilon_2 - \epsilon_j} \right) = \frac{1}{2} H'_{15} H'_{52} \left(\frac{1}{\epsilon_1 - \epsilon_5} + \frac{1}{\epsilon_2 - \epsilon_5} \right) + \frac{1}{2} H'_{16} H'_{62} \left(\frac{1}{\epsilon_1 - \epsilon_6} + \frac{1}{\epsilon_2 - \epsilon_6} \right) \\ &= -\frac{1}{2} eE_x a\, R_r \left(\frac{1}{-\Delta_{02}} + \frac{1}{-\Delta_{02} + Z} \right) + \frac{1}{2} eE_x a\, R_r \left(\frac{1}{-\Delta_{02} - Z} + \frac{1}{-\Delta_{02}} \right) \\ &= eE_x a\, R_r \left(\frac{1}{\Delta_{02}\left(1 - \frac{Z}{\Delta_{02}}\right)} - \frac{1}{\Delta_{02}\left(1 + \frac{Z}{\Delta_{02}}\right)} \right) = (2eE_x a\, R_r Z)/\Delta_{02}^2 + (2eE_x a\, R_r Z^3)/\Delta_{02}^4, \end{aligned} \tag{B19}$$

where we have used $Z = g_\parallel \mu_B B_x$ with in-plane g-factor $g_\parallel \approx 0.22$, $\Delta_{02} = E_2 - E_0$. This gives $\tilde{H}_{12} \propto B_x$ in lowest order, explaining the linear magnetic field dependence of EDSR. The next order of expansion generates $\tilde{H}_{12} \propto B_x^3$. From Eqs. (B16) and (B17), the α_2 term vanishes when $L_x = L_y$, i.e., for a symmetric dot, while it is strongly nonzero for an elliptical dot; making the linear B_x dependence stronger for the latter.

APPENDIX C: BULK PHONON MEDIATED RELAXATION RATE ANALYTICS

The total strain in the 4×4 Luttinger-Kohn-Bir-Pikus formalism is given as

$$H_{\text{strain}}^{\text{LKBP}}(\boldsymbol{r}) = \begin{pmatrix} P_\varepsilon(\boldsymbol{r}) + Q_\varepsilon(\boldsymbol{r}) & 0 & L_\varepsilon(\boldsymbol{r}) & M_\varepsilon(\boldsymbol{r}) \\ 0 & P_\varepsilon(\boldsymbol{r}) + Q_\varepsilon(\boldsymbol{r}) & M_\varepsilon(\boldsymbol{r})^* & -L_\varepsilon(\boldsymbol{r})^* \\ L_\varepsilon(\boldsymbol{r})^* & M_\varepsilon(\boldsymbol{r}) & P_\varepsilon(\boldsymbol{r}) - Q_\varepsilon(\boldsymbol{r}) & 0 \\ M_\varepsilon(\boldsymbol{r})^* & -L_\varepsilon(\boldsymbol{r}) & 0 & P_\varepsilon(\boldsymbol{r}) - Q_\varepsilon(\boldsymbol{r}) \end{pmatrix}, \tag{C1}$$

where $P_\varepsilon(\boldsymbol{r}) = -a(\varepsilon_{xx}(\boldsymbol{r}) + \varepsilon_{yy}(\boldsymbol{r}) + \varepsilon_{zz}(\boldsymbol{r}))$, $Q_\varepsilon(\boldsymbol{r}) = -\frac{b}{2}(\varepsilon_{xx}(\boldsymbol{r}) + \varepsilon_{yy}(\boldsymbol{r}) - 2\varepsilon_{zz}(\boldsymbol{r}))$, $L_\varepsilon(\boldsymbol{r}) = d(\varepsilon_{xz}(\boldsymbol{r}) - i\varepsilon_{yz}(\boldsymbol{r}))$, $M_\varepsilon(\boldsymbol{r}) = (\frac{\sqrt{3}}{2} b(\varepsilon_{xx}(\boldsymbol{r}) - \varepsilon_{yy}(\boldsymbol{r})) - id\varepsilon_{xy}(\boldsymbol{r}))$. The nonzero static component of the strain tensor is given by $\varepsilon_{xx} = \varepsilon_{yy} = -0.006$ and $\varepsilon_{zz} = -\frac{C_{12}}{C_{11}}\varepsilon_{xx}$ with $C_{12} = 44\,\text{GPa}$ and $C_{11} = 126\,\text{GPa}$. Considering the lattice deformation potential $\mathcal{D}(\boldsymbol{r})$, the "local" strain is given by

$$\varepsilon_{i,j}^{\alpha}(\boldsymbol{r}) = \frac{1}{2}\left(\frac{\partial u_i(\boldsymbol{r})}{\partial r_j} + \frac{\partial u_j(\boldsymbol{r})}{\partial r_i} \right), \quad i, j \in \{x, y, z\}. \tag{C2}$$

Here $\boldsymbol{u}$ vector designates the deformation field at the position $\boldsymbol{r}$. For a phonon traveling with wave vector $\mathbf{q}$ in the polarized state α, the strain tensor is given by,

$$\varepsilon_{i,j}^{\alpha}(\boldsymbol{r}) = \frac{i}{2}\sqrt{\frac{\hbar}{2V_c \rho \omega_{\mathbf{q},\alpha}}}\, q(\hat{c}_i^{\alpha}\hat{q}_j + \hat{c}_j^{\alpha}\hat{q}_i)(e^{-i\mathbf{q}\cdot\mathbf{r}} a_{\mathbf{q},\alpha} + e^{i\mathbf{q}\cdot\mathbf{r}} a_{\mathbf{q},\alpha}^{\dagger}), \tag{C3}$$

where $\hat{c}$ is the polar ization unit vector. We consider three polar izations with con-ordinate systems understood as $l : (r, \theta, \phi)$; $t : (r, \theta + \frac{\pi}{2}, \phi)$; $w : (r, \frac{\pi}{2}, \phi + \frac{\pi}{2})$. Using $\omega_{\mathbf{q},\alpha} = v_\alpha q$,

$$\varepsilon_{i,j}^{\alpha}(\boldsymbol{r}) = i\sqrt{\frac{\hbar}{2V_c \rho v_\alpha}}\, \sqrt{q}\, \mathcal{A}_{\varepsilon,ij}^{\alpha} e^{i\mathbf{q}\cdot\mathbf{r}} (a_{-\mathbf{q},\alpha} + a_{\mathbf{q},\alpha}^{\dagger}), \tag{C4}$$

where v_α are the acoustic phonon velocities, and we assumed $\frac{1}{2}(\hat{c}_i^{\alpha}\hat{q}_j + \hat{c}_j^{\alpha}\hat{q}_i) = \mathcal{A}_{\varepsilon,ij}^{\alpha}$. The matrix elements of $\mathcal{A}_{\varepsilon,ij}^{\alpha}$ are sketched out below:

$$\mathcal{A}_{\varepsilon}^{\alpha} = \frac{1}{2}\begin{pmatrix} 2\hat{c}_x^{\alpha}\hat{q}_x & \hat{c}_x^{\alpha}\hat{q}_y + \hat{c}_y^{\alpha}\hat{q}_x & \hat{c}_x^{\alpha}\hat{q}_z + \hat{c}_z^{\alpha}\hat{q}_x \\ \hat{c}_y^{\alpha}\hat{q}_x + \hat{c}_x^{\alpha}\hat{q}_y & 2\hat{c}_y^{\alpha}\hat{q}_y & \hat{c}_y^{\alpha}\hat{q}_z + \hat{c}_z^{\alpha}\hat{q}_y \\ \hat{c}_z^{\alpha}\hat{q}_x + \hat{c}_x^{\alpha}\hat{q}_z & \hat{c}_z^{\alpha}\hat{q}_y + \hat{c}_y^{\alpha}\hat{q}_z & 2\hat{c}_z^{\alpha}\hat{q}_z \end{pmatrix}. \tag{C5}$$

The phonon wave vector has the components $\overrightarrow{q} \rightarrow \{q\sin\theta\cos\phi, q\sin\theta\ \sin\phi, q\cos\theta\}$; so the unit vectors for $\boldsymbol{q}$ are given by: $\hat{q} \rightarrow \{\sin\theta\cos\phi,\ \sin\theta\ \sin\phi,\ \cos\theta\}$. The polarization wave vectors are as follows:

(1) $\hat{c}^l \rightarrow q^{-1}\{q_x, q_y, q_z\} = \{\sin\theta\cos\phi,\ \sin\theta\cos\phi,\ \cos\theta\}$;
(2) $\hat{c}^t \rightarrow q^{-1}(q_x^2+q_y^2)^{-\frac{1}{2}}\{q_xq_z, q_yq_z, -(q_x^2+q_y^2)\} = \{\cos\theta\cos\phi,\ \cos\theta\sin\phi, -\sin\theta\}$;
(3) $\hat{c}^w \rightarrow (q_x^2+q_y^2)^{-\frac{1}{2}}\{q_y, -q_x, 0\} = \{-\sin\phi,\ \cos\phi,\ 0\}$.

We can write the matrix elements of $\mathcal{A}^{\alpha}_{\varepsilon,ij}$ for the three polar izations using the decompositions above:

$$\mathcal{A}^l_\varepsilon = \frac{1}{2}\begin{pmatrix} 2\frac{q_x^2}{q^2} & 2\frac{q_xq_y}{q^2} & 2\frac{q_xq_z}{q^2} \\ 2\frac{q_yq_x}{q^2} & 2\frac{q_y^2}{q^2} & 2\frac{2q_yq_z}{q^2} \\ 2\frac{q_zq_x}{q^2} & 2\frac{q_zq_y}{q^2} & 2\frac{q_z^2}{q^2} \end{pmatrix} = \frac{1}{q^2}\begin{pmatrix} q_x^2 & q_xq_y & q_xq_z \\ q_yq_x & q_y^2 & q_yq_z \\ q_zq_x & q_zq_y & q_z^2 \end{pmatrix},$$

$$\mathcal{A}^t_\varepsilon = \frac{1}{2}\begin{pmatrix} 2\frac{q_z}{q}\frac{q_x}{\sqrt{q_x^2+q_y^2}}\frac{q_x}{q} & 2\frac{q_z}{q}\frac{q_x}{\sqrt{q_x^2+q_y^2}}\frac{q_y}{q} & \frac{q_xq_z}{q\sqrt{q_x^2+q_y^2}}\frac{q_z}{q} - \frac{\sqrt{q_x^2+q_y^2}}{q}\frac{q_x}{q} \\ 2\frac{q_z}{q}\frac{q_x}{\sqrt{q_x^2+q_y^2}}\frac{q_y}{q} & 2\frac{q_z}{q}\frac{q_y}{\sqrt{q_x^2+q_y^2}}\frac{q_y}{q} & \frac{q_yq_z}{q\sqrt{q_x^2+q_y^2}}\frac{q_z}{q} - \frac{\sqrt{q_x^2+q_y^2}}{q}\frac{q_y}{q} \\ \frac{q_xq_z}{q\sqrt{q_x^2+q_y^2}}\frac{q_z}{q} - \frac{\sqrt{q_x^2+q_y^2}}{q}\frac{q_x}{q} & \frac{q_z^2q_y-q_x^2q_y-q_y^3}{q^2\sqrt{q_x^2+q_y^2}} & -2\frac{q_z}{q}\frac{\sqrt{q_x^2+q_y^2}}{q} \end{pmatrix},$$

$$\mathcal{A}^w_\varepsilon = \frac{1}{2}\begin{pmatrix} -2\frac{q_y}{\sqrt{q_x^2+q_y^2}}\frac{q_x}{q} & -\frac{q_y}{\sqrt{q_x^2+q_y^2}}\frac{q_y}{q} + \frac{q_x}{\sqrt{q_x^2+q_y^2}}\frac{q_x}{q} & -\frac{q_y}{\sqrt{q_x^2+q_y^2}}\frac{q_z}{q} \\ \frac{q_x^2-q_y^2}{q\sqrt{q_x^2+q_y^2}} & 2\frac{q_xq_y}{q\sqrt{q_x^2+q_y^2}} & \frac{q_xq_z}{q\sqrt{q_x^2+q_y^2}} \\ -\frac{q_yq_z}{q\sqrt{q_x^2+q_y^2}} & \frac{q_xq_z}{q\sqrt{q_x^2+q_y^2}} & 0 \end{pmatrix}. \tag{C6}$$

We wish to evaluate the angular integrals, so we write the matrices in terms of θ and ϕ:

$$\mathcal{A}^l_\varepsilon = \begin{pmatrix} \sin^2\theta\cos^2\phi & \sin^2\theta\sin\phi\cos\phi & \sin\theta\cos\theta\cos\phi \\ \sin^2\theta\sin\phi\cos\phi & \sin^2\theta\sin^2\phi & \sin\theta\cos\theta\sin\phi \\ \sin\theta\cos\theta\cos\phi & \sin\theta\cos\theta\sin\phi & \cos^2\theta \end{pmatrix},$$

$$\mathcal{A}^t_\varepsilon = \frac{1}{2}\begin{pmatrix} 2\cos\theta\cos\phi\sin\theta\cos\phi & 2\cos\theta\cos\phi\sin\theta\sin\phi & \cos\theta\cos\phi\cos\theta - \sin^2\theta\cos\phi \\ 2\cos\theta\cos\phi\sin\theta\sin\phi & 2\cos\theta\sin\phi\sin\theta\sin\phi & \cos\theta\sin\phi\cos\theta - \sin^2\theta\sin\phi \\ \cos\theta\cos\phi\cos\theta - \sin^2\theta\cos\phi & \cos\theta\sin\phi\cos\theta - \sin^2\theta\sin\phi & -2\sin\theta\cos\theta \end{pmatrix}$$

$$= \begin{pmatrix} \frac{1}{2}\sin2\theta\cos^2\phi & \frac{1}{4}\sin2\theta\sin2\phi & \frac{1}{2}\cos2\theta\cos\phi \\ \frac{1}{4}\sin2\theta\sin2\phi & \frac{1}{2}\sin2\theta\sin^2\phi & \frac{1}{2}\cos2\theta\sin\phi \\ \frac{1}{2}\cos2\theta\cos\phi & \frac{1}{2}\cos2\theta\sin\phi & -\frac{1}{2}\sin2\theta \end{pmatrix},$$

$$\mathcal{A}^w_\varepsilon = \frac{1}{2}\begin{pmatrix} -2\sin\phi\sin\theta\cos\phi & -\sin\phi\sin\theta\sin\phi + \cos\phi\sin\theta\cos\phi & -\sin\phi\cos\theta \\ -\sin\phi\sin\theta\sin\phi + \cos\phi\sin\theta\cos\phi & 2\cos\phi\sin\theta\sin\phi & \cos\phi\cos\theta \\ -\sin\phi\cos\theta & \cos\phi\cos\theta & 0 \end{pmatrix}$$

$$= \frac{1}{2}\begin{pmatrix} -\sin2\phi\sin\theta & \cos2\phi\sin\theta & -\sin\phi\cos\theta \\ \cos2\phi\sin\theta & \sin2\phi\sin\theta & \cos\phi\cos\theta \\ -\sin\phi\cos\theta & \cos\phi\cos\theta & 0 \end{pmatrix}. \tag{C7}$$

The total hole-phonon Hamiltonian can be added as per the following equation:

$$H^{\alpha}_{h-\mathrm{ph}} = \mathcal{D}^{\alpha}_{11}\mathcal{A}^{\alpha}_{\varepsilon,11} + \mathcal{D}^{\alpha}_{12}\mathcal{A}^{\alpha}_{\varepsilon,12} + \mathcal{D}^{\alpha}_{13}\mathcal{A}^{\alpha}_{\varepsilon,13} + \mathcal{D}^{\alpha}_{22}\mathcal{A}^{\alpha}_{\varepsilon,22} + \mathcal{D}^{\alpha}_{23}\mathcal{A}^{\alpha}_{\varepsilon,23} + \mathcal{D}^{\alpha}_{33}\mathcal{A}^{\alpha}_{\varepsilon,33}. \tag{C8}$$

where α is the polar ization index, and $\mathcal{D}$ are the 4×4 LK deformation potential matrices.

a. l polar ization. Putting in the local strain terms, we can write

$$H^l_{h-\mathrm{ph}} = i\sqrt{q}\sqrt{\frac{\hbar}{2V_c\rho v_l}}\begin{pmatrix} P^l_\varepsilon + Q^l_\varepsilon & 0 & L^l_\varepsilon & M^l_\varepsilon \\ 0 & P^l_\varepsilon + Q^l_\varepsilon & M^{l*}_\varepsilon & -L^{l*}_\varepsilon \\ L^{l*}_\varepsilon & M^l_\varepsilon & P^l_\varepsilon - Q^l_\varepsilon & 0 \\ M^{l*}_\varepsilon & -L^l_\varepsilon & 0 & P^l_\varepsilon - Q^l_\varepsilon \end{pmatrix} e^{i\mathbf{q}\cdot\mathbf{r}}(a_{-\mathbf{q},l} + a^{\dagger}_{\mathbf{q},l}),$$

where

$$P^l_\varepsilon = -a(\sin^2\theta\cos^2\phi + \sin^2\theta\sin^2\phi + \cos^2\theta) = -a,$$

$$Q^l_\varepsilon = -\frac{b}{2}(\sin^2\theta\cos^2\phi + \sin^2\theta\sin^2\phi - 2\cos^2\theta) = -\frac{b}{2}(1 - 3\cos^2\theta),$$

$$L_\varepsilon^l = d(\sin\theta\cos\theta\cos\phi - i\sin\theta\cos\theta\sin\phi) = \frac{d}{2}\sin 2\theta\, e^{-i\phi},$$

$$M_\varepsilon^l = \frac{\sqrt{3}b}{2}(\sin^2\theta\cos^2\phi - \sin^2\theta\sin^2\phi) - id\sin\phi\cos\phi\sin^2\theta = \frac{\sqrt{3}b}{2}\sin^2\theta\cos 2\phi - \frac{id}{2}\sin 2\phi\sin^2\theta. \tag{C9}$$

b. t polar ization. The hole-phonon Hamiltonian in this case takes the following form in angular coordinates:

$$H_{h-\mathrm{ph}}^t = i\sqrt{q}\sqrt{\frac{\hbar}{2V_c\rho v_t}}\begin{pmatrix} P_\varepsilon^t + Q_\varepsilon^t & 0 & L_\varepsilon^t & M_\varepsilon^t \\ 0 & P_\varepsilon^t + Q_\varepsilon^t & M_\varepsilon^{t^*} & -L_\varepsilon^{t^*} \\ L_\varepsilon^{t^*} & M_\varepsilon^t & P_\varepsilon^t - Q_\varepsilon^t & 0 \\ M_\varepsilon^{t^*} & -L_\varepsilon^t & 0 & P_\varepsilon^t - Q_\varepsilon^t \end{pmatrix} e^{i\mathbf{q}\cdot\mathbf{r}}(a_{-\mathbf{q},t} + a_{\mathbf{q},t}^\dagger),$$

where

$$P_\varepsilon^t = -a\left(\frac{1}{2}\sin 2\theta\cos^2\phi + \frac{1}{2}\sin 2\theta\sin^2\phi - \frac{1}{2}\sin 2\theta\right) = 0,$$

$$Q_\varepsilon^t = -\frac{b}{2}\left(\frac{1}{2}\sin 2\theta\cos^2\phi + \frac{1}{2}\sin 2\theta\sin^2\phi + \sin 2\theta\right) = -\frac{3b}{4}\sin 2\theta,$$

$$L_\varepsilon^t = d\left(\frac{1}{2}\cos 2\theta\cos\phi - \frac{i}{2}\cos 2\theta\sin\phi\right) = \frac{d}{2}\cos 2\theta e^{-i\phi},$$

$$M_\varepsilon^t = \frac{\sqrt{3}b}{2}\left(\frac{1}{2}\sin 2\theta\cos^2\phi - \frac{1}{2}\sin 2\theta\sin^2\phi\right) - \frac{id}{4}\sin 2\theta\sin 2\phi = \frac{\sqrt{3}b}{4}\sin 2\theta\cos 2\phi - \frac{id}{4}\sin 2\theta\sin 2\phi. \tag{C10}$$

c. w polar ization. For the third polarization direction:

$$H_{h-\mathrm{ph}}^w = i\sqrt{q}\sqrt{\frac{\hbar}{2V_c\rho v_w}}\begin{pmatrix} P_\varepsilon^w + Q_\varepsilon^w & 0 & L_\varepsilon^w & M_\varepsilon^w \\ 0 & P_\varepsilon^w + Q_\varepsilon^w & M_\varepsilon^{w^*} & -L_\varepsilon^{w^*} \\ L_\varepsilon^{w^*} & M_\varepsilon^w & P_\varepsilon^w - Q_\varepsilon^w & 0 \\ M_\varepsilon^{w^*} & -L_\varepsilon^w & 0 & P_\varepsilon^w - Q_\varepsilon^w \end{pmatrix} e^{i\mathbf{q}\cdot\mathbf{r}}(a_{-\mathbf{q},w} + a_{\mathbf{q},w}^\dagger),$$

where

$$P_\varepsilon^w = -a\left(-\frac{1}{2}\sin 2\phi\sin\theta + \frac{1}{2}\sin 2\phi\sin\theta\right) = 0,$$

$$Q_\varepsilon^w = -\frac{b}{2}\left(-\frac{1}{2}\sin 2\phi\sin\theta + \frac{1}{2}\sin 2\phi\sin\theta\right) = 0,$$

$$L_\varepsilon^w = d\left(-\frac{1}{2}\sin\phi\cos\theta - \frac{i}{2}\cos\phi\cos\theta\right) = -\frac{id}{2}\cos\theta e^{-i\phi},$$

$$M_\varepsilon^w = \frac{\sqrt{3}b}{2}\left(-\frac{1}{2}\sin 2\phi\sin\theta - \frac{1}{2}\sin 2\phi\sin\theta\right) - \frac{id}{2}\cos 2\phi\sin\theta = -\frac{\sqrt{3}b}{2}\sin 2\phi\sin\theta - \frac{id}{2}\cos 2\phi\sin\theta. \tag{C11}$$

The relaxation rate is characterized by the spontaneous and stimulated phonon scattering, hence:

$$\Gamma_1 = \frac{1}{T_1} = \sum_\alpha\left(\frac{2\pi}{\hbar}\sum_{\mathbf{q}}|\langle\mathbb{0}|H_{h-\mathrm{ph}}|\mathbb{1}\rangle_\alpha|^2\delta\big(\Delta\mathbb{E} - \hbar\omega_{\alpha,\mathbf{q}}\big)\right). \tag{C12}$$

The summation over the wave vectors can be changed to continuous integral, and the creation-annihilation operators can be approximated to produce a factor of N_q, which denotes the number of acoustic phonons with q momentum:

$$\begin{aligned}\Gamma_1 = \frac{1}{T_1} &= \sum_\alpha\left(\frac{2\pi}{\hbar}\frac{\cancel{V}}{(2\pi)3}\int_{V_q} d^3\mathbf{q}\, q\frac{\cancel{\hbar}}{2\cancel{V_c}\rho v_\alpha}\left|\langle\mathbb{0}|e^{i\mathbf{q}\cdot\mathbf{r}}H_{\mathrm{strain},\alpha}^{\mathrm{LKBP}}\cancel{N_q}|\mathbb{1}\rangle_\alpha\right|^2\delta(\Delta\mathbb{E} - \hbar v_\alpha q)\right) \\ &= \sum_\alpha\left(\frac{1}{8\pi^2}\int_{V_q} q^3\, dq\, \sin\theta\, d\theta\, d\phi\frac{1}{\rho v_\alpha}\left|\langle\mathbb{0}|e^{i\mathbf{q}\cdot\mathbf{r}}H_{\mathrm{strain},\alpha}^{\mathrm{LKBP}}|\mathbb{1}\rangle_\alpha\right|^2\frac{1}{\hbar v_\alpha}\delta\left(\frac{\Delta\mathbb{E}}{\hbar v_\alpha} - q\right)\right) \\ &= \sum_\alpha\left(\frac{1}{8\pi^2\hbar\rho v_\alpha^2}\int_0^{2\pi} d\phi\int_0^{\pi} d\theta\sin\theta\int_0^{\infty} q^3 dq\left|\langle\mathbb{0}|e^{i\mathbf{q}\cdot\mathbf{r}}H_{\mathrm{strain},\alpha}^{\mathrm{LKBP}}|\mathbb{1}\rangle_\alpha\right|^2\delta\left(\frac{\Delta\mathbb{E}}{\hbar v_\alpha} - q\right)\right).\end{aligned} \tag{C13}$$

The qubit ground state $|\mathbb{0}\rangle$ and excited state $|\mathbb{1}\rangle$ are 1×4 spinors with each component multiplied to spatial functions.

$$\Rightarrow \langle \mathbb{0}|e^{i\mathbf{q}\cdot\mathbf{r}}H^{\mathrm{LKBP}}_{\mathrm{strain},\alpha}|\mathbb{1}\rangle = (g_1^* \quad g_2^* \quad g_3^* \quad g_4^*)e^{i\mathbf{q}\cdot\mathbf{r}}\begin{pmatrix} P_\varepsilon^\alpha+Q_\varepsilon^\alpha & 0 & L_\varepsilon^\alpha & M_\varepsilon^\alpha \\ 0 & P_\varepsilon^\alpha+Q_\varepsilon^\alpha & M_\varepsilon^{\alpha^*} & -L_\varepsilon^{\alpha^*} \\ L_\varepsilon^{\alpha^*} & M_\varepsilon^\alpha & P_\varepsilon^\alpha-Q_\varepsilon^\alpha & 0 \\ M_\varepsilon^{\alpha^*} & -L_\varepsilon^\alpha & 0 & P_\varepsilon^\alpha-Q_\varepsilon^\alpha \end{pmatrix}\begin{pmatrix} e_1 \\ e_2 \\ e_3 \\ e_4 \end{pmatrix}$$

$$= (g_1^* \quad g_2^* \quad g_3^* \quad g_4^*)e^{i\mathbf{q}\cdot\mathbf{r}}\begin{pmatrix} \left(P_\varepsilon^\alpha+Q_\varepsilon^\alpha\right)e_1 + L_\varepsilon^\alpha e_3 + M_\varepsilon^\alpha e_4 \\ \left(P_\varepsilon^\alpha+Q_\varepsilon^\alpha\right)e_2 + M_\varepsilon^{\alpha^*} e_3 - L_\varepsilon^{\alpha^*} e_4 \\ L_\varepsilon^{\alpha^*} e_1 + M_\varepsilon^\alpha e_2 + \left(P_\varepsilon^\alpha-Q_\varepsilon^\alpha\right)e_3 \\ M_\varepsilon^{\alpha^*} e_1 - L_\varepsilon^\alpha e_2 + \left(P_\varepsilon^\alpha-Q_\varepsilon^\alpha\right)e_4 \end{pmatrix}$$

$$= \Big[\Big\{\left(P_\varepsilon^\alpha+Q_\varepsilon^\alpha\right)e^{i\mathbf{q}\cdot\mathbf{r}}g_1^*e_1 + L_\varepsilon^\alpha e^{i\mathbf{q}\cdot\mathbf{r}}g_1^*e_3 + M_\varepsilon^\alpha e^{i\mathbf{q}\cdot\mathbf{r}}g_1^*e_4\Big\} + \Big\{\left(P_\varepsilon^\alpha+Q_\varepsilon^\alpha\right)e^{i\mathbf{q}\cdot\mathbf{r}}g_2^*e_2 + M_\varepsilon^{\alpha^*}e^{i\mathbf{q}\cdot\mathbf{r}}g_2^*e_3 - L_\varepsilon^{\alpha^*}e^{i\mathbf{q}\cdot\mathbf{r}}g_2^*e_4\Big\}$$
$$+\Big\{L_\varepsilon^{\alpha^*}e^{i\mathbf{q}\cdot\mathbf{r}}g_3^*e_1 + M_\varepsilon^\alpha e^{i\mathbf{q}\cdot\mathbf{r}}g_3^*e_2 + \left(P_\varepsilon^\alpha-Q_\varepsilon^\alpha\right)e^{i\mathbf{q}\cdot\mathbf{r}}g_3^*e_3\Big\} + \Big\{M_\varepsilon^{\alpha^*}e^{i\mathbf{q}\cdot\mathbf{r}}g_4^*e_1 - L_\varepsilon^\alpha e^{i\mathbf{q}\cdot\mathbf{r}}g_4^*e_2 + \left(P_\varepsilon^\alpha-Q_\varepsilon^\alpha\right)e^{i\mathbf{q}\cdot\mathbf{r}}g_4^*e_4\Big\}\Big]. \quad \text{(C14)}$$

According to our model $g_i^* = \sum_{\{m,n,l,i'\}} c_{ii'}^{g^*}\psi_n(x)\psi_m(y)\psi_l(z)$, and $e_j^* = \sum_{\{m',n',l',j'\}} c_{jj'}^{e}\psi_{n'}(x)\psi_{m'}(y)\psi_{l'}(z)$; implies that the terms in Eq. (C14) have the form

$$e^{i\mathbf{q}\cdot\mathbf{r}}g_i^*e_j \Rightarrow \left(\sum_{i',j'} c_{ii'}^{g^*}c_{jj'}^{e}\right)\left(\sum_{n,n'}\sum_{m,m'}\sum_{l,l'}\right)\int_{-\infty}^{\infty} dx\, e^{iq_xx}\psi_n(x)\psi_{n'}(x)\int_{-\infty}^{\infty} dy\, e^{iq_yy}\psi_m(y)\psi_{m'}(y)\int_{-\infty}^{\infty} dz\, e^{iq_zz}\psi_l(z)\psi_{l'}(z). \quad \text{(C15)}$$

To our advantage, the inversion-symmetric basis wave functions we use to describe our hole QD, i.e., an infinite barrier in z and harmonic potential in x-y, have closed form solutions of the $e^{i\mathbf{q}\cdot\mathbf{r}}$ integrals. This allows us to evaluate the Relaxation rate Γ_1 analytically. We also show the dipole approximation to agree with the analytical results for T_1; thirdly, a numerical pathway is sketched as an alternative.

Analytical: in-plane integrals. The matrix elements of e^{iq_xx} between two x(or y) wavefunctions are given by

$$\langle n|e^{iq_xx}|n'\rangle = \int_{-\infty}^{\infty} dx\, e^{iq_xx}\psi_n(x)\psi_{n'}(x). \quad \text{(C16)}$$

e^{iq_xx} can be written as an infinite expansion in Hermite polynomial basis:

$$e^{iq_xx} = e^{iq_xL_x\frac{x}{L_x}} = e^{\frac{(-iq_xL_x)^2}{4}}\sum_{r=0}^{\infty}\frac{(iq_xL_x)^r}{2^r r!}H_r\left(\frac{x}{L_x}\right) \quad \text{(C17)}$$

$$\Rightarrow \langle n|e^{iq_xx}|n'\rangle = \frac{1}{\sqrt{2^n n! L_x\sqrt{\pi}}}\frac{1}{\sqrt{2^{n'}n'!L_x\sqrt{\pi}}}e^{-\frac{q_x^2L_x^2}{4}}\sum_{r=0}^{\infty}\frac{(iq_xL_x)^r}{2^r r!}\mathbb{I}(r,n,n') \quad \text{(C18)}$$

with $\mathbb{I}(r,n,n') = \int_{-\infty}^{\infty} dx\, e^{-\frac{x^2}{L_x^2}}H_r(\frac{x}{L_x})H_n(\frac{x}{L_x})H_{n'}(\frac{x}{L_x}) = L_x\int_{-\infty}^{\infty} d(\frac{x}{L_x})\, e^{-\frac{x^2}{L_x^2}}H_r(\frac{x}{L_x})H_n(\frac{x}{L_x})H_{n'}(\frac{x}{L_x})$. Substituting $\frac{x}{L_x}\to x$, we write

$$\Rightarrow \langle n|e^{iq_xx}|n'\rangle = (2^{n+n'}n!n'!\pi)^{-\frac{1}{2}}e^{-\frac{q_x^2L_x^2}{4}}\sum_{r=0}^{\infty}\frac{(iq_xL_x)^r}{2^r r!}\int_{-\infty}^{\infty} dx\, e^{-x^2}H_r(x)H_n(x)H_{n'}(x). \quad \text{(C19)}$$

The product of two Hermite polynomials can be expanded in the Hermite polynomial basis:

$$H_n(x)H_{n'}(x) = 2^n n!n'!\sum_{k=0}^{n}\frac{H_{2k+n'-n}(x)}{2^k k!(k+n'-n)!(n-k)!} \quad \text{(C20)}$$

$$\Rightarrow \langle n|e^{iq_xx}|n'\rangle = \frac{e^{-\frac{q_x^2L_x^2}{4}}}{\sqrt{2^{n+n'}n!n'!\pi}}\sum_{r=0}^{\infty}\frac{(iq_xL_x)^r}{2^r r!}2^n n!n'!\sum_{k=0}^{n}\frac{1}{2^k k!(k+n'-n)!(n-k)!}\int_{-\infty}^{\infty} dx\, e^{-x^2}H_r(x)H_{2k+n'-n}(x)$$

$$= \frac{e^{-\frac{q_x^2L_x^2}{4}}}{\sqrt{2^{n+n'}n!n'!\pi}}\sum_{r=0}^{\infty}\frac{(iq_xL_x)^r}{2^r r!}2^n n!n'!\sum_{k=0}^{n}\frac{2^{2k+n'-n}(2k+n'-n)!\sqrt{\pi}\delta_{r,2k+n'-n}}{2^k k!(k+n'-n)!(n-k)!}, \quad \text{(C21)}$$

where we have used the orthonormality relation: $\int_{-\infty}^{\infty} e^{-x^2} H_n(x) H_{n'}(x)\, dx = 2^n n! \sqrt{\pi}\delta_{n,n'}$. The δ-function boils the r-sum down to only one term, such that

$$\begin{aligned}
&\Rightarrow \langle n|e^{iq_x x}|n'\rangle = \sqrt{\frac{n'!n!}{2^{n'-n}}} e^{-\frac{q_x^2 L_x^2}{4}} \sum_{k=0}^{n} \frac{(iq_x L_x)^{2k+n'-n}}{\cancel{2^{2k+n'-n}}\cancel{(2k+n'-n)!}} \frac{\cancel{2^{2k+n'-n}}\cancel{(2k+n'-n)!}}{2^k k!(k+n'-n)!(n-k)!} \\
&= \sqrt{\frac{n!}{2^{n'-n}n'!}} e^{-\frac{q_x^2 L_x^2}{4}} \sum_{k=0}^{n} \frac{n'!(iq_x L_x)^{n'-n}(iq_x L_x)^{2k}}{2^k k!(k+n'-n)!(n-k)!} = \sqrt{\frac{n!}{2^{n'-n}n'!}} e^{-\frac{q_x^2 L_x^2}{4}} (iq_x L_x)^{n'-n} \sum_{k=0}^{n} \frac{n'!((iq_x L_x)^2)^k}{2^k k!(k+n'-n)!(n-k)!} \\
&= \sqrt{\frac{n!}{2^{n'-n}n'!}} e^{-\frac{q_x^2 L_x^2}{4}} (iq_x L_x)^{n'-n} \sum_{k=0}^{n} \frac{(-1)^k (n+n'-n)!}{k!(k+n'-n)!(n-k)!} \left(\frac{q_x^2 L_x^2}{2}\right)^k.
\end{aligned} \tag{C22}$$

Using the formula for the associated Laguerre polynomial $\mathcal{L}_n^a(x) = \sum_{k=0}^{n} \frac{(-1)^k (n+a)!}{k!(k+a)!(n-k)!} x^k$, the matrix element of $e^{iq_x x}$ can be analytically evaluated as

$$\begin{aligned}
&\Rightarrow \langle n|e^{iq_x x}|n'\rangle = \sqrt{\frac{1}{2^{n'-n}} \frac{n!}{n'!}} e^{-\frac{q_x^2 L_x^2}{4}} (iq_x L_x)^{n'-n} \mathcal{L}_n^{n'-n}\left(\frac{q_x^2 L_x^2}{2}\right) \\
&\Rightarrow \langle m|e^{iq_y y}|m'\rangle = \sqrt{\frac{1}{2^{m'-m}} \frac{m!}{m'!}} e^{-\frac{q_y^2 L_y^2}{4}} (iq_y L_y)^{m'-m} \mathcal{L}_m^{m'-m}\left(\frac{q_y^2 L_y^2}{2}\right).
\end{aligned} \tag{C23}$$

The z-basis wave functions are

$$\psi_l(z) = \begin{cases} \cos\left(\frac{(l+1)\pi z}{L_z}\right) & l = 0, 2, 4, \ldots \\ \sin\left(\frac{(l+1)\pi z}{L_z}\right) & l = 1, 3, 5 \ldots \end{cases}, z \in \left\{-\frac{L_z}{2}, \frac{L_z}{2}\right\}. \tag{C24}$$

The matrix element $\langle l|e^{iq_z z}|l'\rangle$ is evaluated as

$$\int_{-\frac{L_z}{2}}^{\frac{L_z}{2}} dz\, e^{iq_z z} \psi_l(z) \psi_{l'}(z) = \int_{-\frac{L_z}{2}}^{\frac{L_z}{2}} dz\, (\cos q_z z + i \sin q_z z) \psi_r(z) \psi_{r'}(z), \tag{C25}$$

where $r = l + 1$ is the new index for z integral (for simpler mathematical expressions).

r odd, r′ even. For the case of evaluating the matrix element between even and odd z-basis functions is calculated as

$$\begin{aligned}
&= \int_{-\frac{L_z}{2}}^{\frac{L_z}{2}} dz (\cos q_z z + i \sin q_z z) \sqrt{\frac{2}{L_z}} \cos\left(\frac{r\pi z}{L_z}\right) \sqrt{\frac{2}{L_z}} \sin\left(\frac{r'\pi z}{L_z}\right) \\
&= \frac{2}{L_z} \int_{-\frac{L_z}{2}}^{\frac{L_z}{2}} dz (\cos q_z z + i \sin q_z z) \frac{1}{2} \left(\sin\left(\frac{\overline{r+r'}\pi z}{L_z}\right) - \sin\left(\frac{\overline{r-r'}\pi z}{L_z}\right)\right) \\
&= \frac{1}{L_z} \int_{-\frac{L_z}{2}}^{\frac{L_z}{2}} dz \left(\cos q_z z \sin\left(\frac{\overline{r+r'}\pi z}{L_z}\right) - \cos q_z z \sin\left(\frac{\overline{r-r'}\pi z}{L_z}\right) + i \sin q_z z \sin\left(\frac{\overline{r+r'}\pi z}{L_z}\right) - i \sin q_z z \sin\left(\frac{\overline{r-r'}\pi z}{L_z}\right)\right) \\
&= \frac{1}{2L_z} \int_{-\frac{L_z}{2}}^{\frac{L_z}{2}} dz \left(\sin\left(q_z z + \frac{\overline{r+r'}\pi z}{L_z}\right) - \sin\left(q_z z - \frac{\overline{r+r'}\pi z}{L_z}\right) - \sin\left(q_z z + \frac{\overline{r-r'}\pi z}{L_z}\right) + \sin\left(q_z z - \frac{\overline{r-r'}\pi z}{L_z}\right)\right) \\
&\quad + \frac{i}{2L_z} \int_{-\frac{L_z}{2}}^{\frac{L_z}{2}} dz \left(\cos\left(q_z z + \frac{\overline{r+r'}\pi z}{L_z}\right) + \cos\left(q_z z - \frac{\overline{r+r'}\pi z}{L_z}\right) - \cos\left(q_z z + \frac{\overline{r-r'}\pi z}{L_z}\right) - \sin\left(q_z z - \frac{\overline{r-r'}\pi z}{L_z}\right)\right).
\end{aligned} \tag{C26}$$

The sin and cos terms can be now evaluated straight forwardly to give us the final simplified expression:

$$= \frac{i}{2} \left[\frac{\sin\left(\frac{q_z L_z}{2} + \frac{(r+r')\pi}{2}\right)}{\frac{q_z L_z}{2} + \frac{(r+r')\pi}{2}} - \frac{\sin\left(\frac{q_z L_z}{2} - \frac{(r+r')\pi}{2}\right)}{\frac{q_z L_z}{2} - \frac{(r+r')\pi}{2}} - \frac{\sin\left(\frac{q_z L_z}{2} + \frac{(r-r')\pi}{2}\right)}{\frac{q_z L_z}{2} + \frac{(r-r')\pi}{2}} + \frac{\sin\left(\frac{q_z L_z}{2} - \frac{(r-r')\pi}{2}\right)}{\frac{q_z L_z}{2} - \frac{(r-r')\pi}{2}} \right]. \tag{C27}$$

r, r′ both odd/even. For the case of evaluating the matrix element between both even(both odd) z-basis functions is calculated as

$$= \int_{-\frac{L_z}{2}}^{\frac{L_z}{2}} dz(\cos q_z z + i \sin q_z z)\sqrt{\frac{2}{L_z}}\sin\left(\frac{r\pi z}{L_z}\right)\sqrt{\frac{2}{L_z}}\sin\left(\frac{r'\pi z}{L_z}\right)$$
$$= -\frac{1}{2}\left[\frac{\sin\left(\frac{q_z L_z}{2}+\frac{(r+r')\pi}{2}\right)}{\frac{q_z L_z}{2}+\frac{(r+r')\pi}{2}} + \frac{\sin\left(\frac{q_z L_z}{2}-\frac{(r+r')\pi}{2}\right)}{\frac{q_z L_z}{2}-\frac{(r+r')\pi}{2}} + \frac{\sin\left(\frac{q_z L_z}{2}+\frac{(r-r')\pi}{2}\right)}{\frac{q_z L_z}{2}+\frac{(r-r')\pi}{2}} + \frac{\sin\left(\frac{q_z L_z}{2}-\frac{(r-r')\pi}{2}\right)}{\frac{q_z L_z}{2}-\frac{(r-r')\pi}{2}}\right]. \tag{C28}$$

Finally we put the results from Eqs. (C23) and (C28) into Eq. (C15) to evaluate:

$$e^{i\mathbf{q}\cdot\mathbf{r}} g_i^* e_j \Rightarrow \left(\sum_{i',j'} c_{ii'}^{g^*} c_{jj'}^{e}\right)\left(\sum_{n,n'}\sum_{m,m'}\sum_{l,l'}\right)\sqrt{\frac{1}{2^{n'-n}}\frac{n!}{n'!}}e^{-\frac{q_x^2 L_x^2}{4}}(iq_x L_x)^{n'-n}\mathcal{L}_n^{n'-n}\left(\frac{q_x^2 L_x^2}{2}\right)$$
$$\times\sqrt{\frac{1}{2^{m'-m}}\frac{m!}{m'!}}e^{-\frac{q_y^2 L_y^2}{4}}(iq_y L_y)^{m'-m}\mathcal{L}_m^{m'-m}\left(\frac{q_y^2 L_y^2}{2}\right)\times f(l,l',q_z L_z), \tag{C29}$$

where

$$f(l,l',q_z L_z) = \begin{cases} \frac{i}{2}\left[\frac{\sin\left(\frac{q_z L_z}{2}+\frac{(r+r')\pi}{2}\right)}{\frac{q_z L_z}{2}+\frac{(r+r')\pi}{2}} - \frac{\sin\left(\frac{q_z L_z}{2}-\frac{(r+r')\pi}{2}\right)}{\frac{q_z L_z}{2}-\frac{(r+r')\pi}{2}} - \frac{\sin\left(\frac{q_z L_z}{2}+\frac{(r-r')\pi}{2}\right)}{\frac{q_z L_z}{2}+\frac{(r-r')\pi}{2}} + \frac{\sin\left(\frac{q_z L_z}{2}-\frac{(r-r')\pi}{2}\right)}{\frac{q_z L_z}{2}-\frac{(r-r')\pi}{2}}\right] & l\pm l' = \text{odd} \\ -\frac{1}{2}\left[\frac{\sin\left(\frac{q_z L_z}{2}+\frac{(r+r')\pi}{2}\right)}{\frac{q_z L_z}{2}+\frac{(r+r')\pi}{2}} + \frac{\sin\left(\frac{q_z L_z}{2}-\frac{(r+r')\pi}{2}\right)}{\frac{q_z L_z}{2}-\frac{(r+r')\pi}{2}} + \frac{\sin\left(\frac{q_z L_z}{2}+\frac{(r-r')\pi}{2}\right)}{\frac{q_z L_z}{2}+\frac{(r-r')\pi}{2}} + \frac{\sin\left(\frac{q_z L_z}{2}-\frac{(r-r')\pi}{2}\right)}{\frac{q_z L_z}{2}-\frac{(r-r')\pi}{2}}\right] & l\pm l' = \text{even} \end{cases}. \tag{C30}$$

Next we make the substitution $q_x \to q\sin\theta\cos\phi$, $q_y \to q\sin\theta\sin\phi$, $q_z \to q\cos\theta$ to write

$$e^{i\mathbf{q}\cdot\mathbf{r}} g_i^* e_j \Rightarrow \left(\sum_{i',j'} c_{ii'}^{g^*} c_{jj'}^{e}\right)\left(\sum_{n,n'}\sum_{m,m'}\sum_{l,l'}\right)\sqrt{\frac{1}{2^{n'-n}}\frac{n!}{n'!}}e^{-\frac{q^2 L_x^2 \sin^2\theta\cos^2\phi}{4}}(iqL_x\sin\theta\cos\phi)^{n'-n}\mathcal{L}_n^{n'-n}\left(\frac{q^2 L_x^2\sin^2\theta\cos^2\phi}{2}\right)$$
$$\times\sqrt{\frac{1}{2^{m'-m}}\frac{m!}{m'!}}e^{-\frac{q^2 L_y^2\sin^2\theta\sin^2\phi}{4}}(iqL_y\sin\theta\sin\phi)^{m'-m}\mathcal{L}_m^{m'-m}\left(\frac{q^2 L_y^2\sin^2\theta\sin^2\phi}{2}\right)\times f(l,l',qL_z\cos\theta). \tag{C31}$$

These set of equations allow us to calculate the terms in Eq. (C14) to express $|\langle\mathbb{0}|e^{i\mathbf{q}\cdot\mathbf{r}}H^{\text{LKBP}}_{\text{strain},\alpha}|\mathbb{1}\rangle|^2$ as $I_\alpha(q,\theta,\phi)$. From Eq. (C13),

$$\Gamma_1 = \frac{1}{T_1} = \sum_\alpha\left(\frac{1}{8\pi^2\hbar\rho v_\alpha^2}\int_0^{2\pi}d\phi\int_0^{\pi}d\theta\sin\theta\int_0^{\infty}q^3 dq\, I_\alpha(q,\theta,\phi)\,\delta\left(\frac{\Delta\mathbb{E}}{\hbar v_\alpha}-q\right)\right)$$
$$= \sum_\alpha\left(\frac{\Delta\mathbb{E}^3}{8\pi^2\hbar^4\rho v_\alpha^5}\int_0^{2\pi}d\phi\int_0^{\pi}d\theta\sin\theta\, I_\alpha\left(q\to\frac{\Delta\mathbb{E}}{\hbar v_\alpha},\theta,\phi\right)\right) = \sum_\alpha\left(\frac{\Delta\mathbb{E}^3}{8\pi^2\hbar^4\rho v_\alpha^5}\,\Omega_\alpha\left(\frac{\Delta\mathbb{E}}{\hbar v_\alpha}\right)\right), \tag{C32}$$

where Ω denotes the angular integration.

Dipole approximation. Alternatively, one can expand $e^{i\mathbf{q}\cdot\mathbf{r}} \approx 1(+i\mathbf{q}\cdot\mathbf{r} - |\mathbf{q}\cdot\mathbf{r}|^2 + \dots)$ which simplifies the product $|\langle\mathbb{0}|e^{i\mathbf{q}\cdot\mathbf{r}}H^{\text{LKBP}}_{\text{strain},\alpha}|\mathbb{1}\rangle|^2 \approx |\langle\mathbb{0}|H^{\text{LKBP}}_{\text{strain},\alpha}|\mathbb{1}\rangle + i\langle\mathbb{0}|\mathbf{q}\cdot\mathbf{r}H^{\text{LKBP}}_{\text{strain},\alpha}|\mathbb{1}\rangle - \langle\mathbb{0}||\mathbf{q}\cdot\mathbf{r}|^2 H^{\text{LKBP}}_{\text{strain},\alpha}|\mathbb{1}\rangle + \dots|^2$. In sharp contrast to electron spin-1/2 qubits, where the local strain is a diagonal tensor and the leading zeroth order term $\langle\mathbb{0}|H_\varepsilon|\mathbb{1}\rangle$ vanishes; for the spin-3/2 holes the leading term is the zeroth order, resulting in a $\alpha_r B^3 + \beta_r B^4 + \gamma_r B^5$ relaxation rate variation, compared to B^5 variation in electron spin-1/2 qubits. While the B^3 and B^5 dependence are explained by the first two terms in dipole approximation, the orbital B terms in the qubit admixture give rise to the B^4 dependence.

APPENDIX D: RANDOM TELEGRAPH NOISE(RTN) DEPHASING: SCREENED POTENTIAL OF A CHARGE DEFECT

Taking into account the screening effect of the 2DHG being formed in Ge, the Fourier q-space form of the potential of single defect with charge e is given by

$$U_{scr}(q) = \frac{e^2}{2\epsilon_0\epsilon_r}e^{-qd}\frac{\Theta(2k_F - q)}{q + q_{TF}}, \tag{D1}$$

where $U_{scr}(q)$ is known as the Thomas-Fermi screened potential, q is the Fourier space variable, $q_{\text{TF}} = 0.49\ \text{nm}^{-1}$ is the Thomas-Fermi wave vector in germanium independent of the density of holes. k_F is the Fermi wave vector which is estimated to be $0.1\ \text{nm}^{-1}$ in our calculations, and Θ is the Heaviside theta step function. Considering constant screening, which only holds for

$q<2k_F$, the screened potential in real space under the limit $d \ll r$ is approximated to be

$$U_s(\boldsymbol{r}) = \frac{e^2}{4\pi\epsilon_0\epsilon_r}\frac{1}{q_{\mathrm{TF}}^2}\left(\frac{1}{|\mathbf{r}-\mathbf{r}_D|^3} + d\frac{q_{\mathrm{TF}}}{|\mathbf{r}-\mathbf{r}_D|^3}\right). \tag{D2}$$

The relative electrical permeability of germanium is $\epsilon_r = 15.8$; ϵ_0 being the vacuum electrical permeability. $\mathbf{r}_D = \{80\ \mathrm{nm}, 80\ \mathrm{nm}, 0\}$ is the vector denoting the distance of the in-plane charge defect from the center of the QD.

APPENDIX E: *g*-FACTOR ANISOTROPY AND FITTING PARAMETERS

In the main text, Fig. 8, we mentioned that the fitting paramters are not unique. Here we suggest some other possible configurations to fit the parameters. The main fitting parameters are dot size (L_x, L_y, L_z), the electric field can be tuned via gate to modulate the g-factors.

(1) $L_x = 40$ nm, $L_y = 60$ nm, $L_z = 10$ nm.
(2) $L_x = 30$ nm, $L_y = 50$ nm, $L_z = 10.5$ nm.
(3) $L_x = 44$ nm, $L_y = 60$ nm, $L_z = 9.5$ nm.

Note that there are many other possible combinations of parameters if the strains (both uniaxial strain and shear strain) are included.

[1] B. E. Kane, Nature (London) **393**, 133 (1998).
[2] D. Loss and D. P. DiVincenzo, Phys. Rev. A **57**, 120 (1998).
[3] J. R. Petta, A. C. Johnson, J. M. Taylor, E. A. Laird, A. Yacoby, M. D. Lukin, C. M. Marcus, M. P. Hanson, and A. C. Gossard, Science **309**, 2180 (2005).
[4] R. Hanson, L. P. Kouwenhoven, J. R. Petta, S. Tarucha, and L. M. K. Vandersypen, Rev. Mod. Phys. **79**, 1217 (2007).
[5] R. Hanson and D. D. Awschalom, Nature (London) **453**, 1043 (2008).
[6] F. A. Zwanenburg, A. S. Dzurak, A. Morello, M. Y. Simmons, L. C. L. Hollenberg, G. Klimeck, S. Rogge, S. N. Coppersmith, and M. A. Eriksson, Rev. Mod. Phys. **85**, 961 (2013).
[7] A. Chatterjee, P. Stevenson, S. De Franceschi, A. Morello, N. P. de Leon, and F. Kuemmeth, Nat. Rev. Phys. **3**, 157 (2021).
[8] G. Scappucci, C. Kloeffel, F. A. Zwanenburg, D. Loss, M. Myronov, J.-J. Zhang, S. De Franceschi, G. Katsaros, and M. Veldhorst, Nat. Rev. Mater. **6**, 926 (2021).
[9] Y. Fang, P. Philippopoulos, D. Culcer, W. Coish, and S. Chesi, Mater. Quantum. Technol. **3**, 012003 (2023).
[10] M. Cardona and Y. Y. Peter, *Fundamentals of Semiconductors* (Springer, Berlin, Germany, 2005), Vol. 619.
[11] K. Itoh, W. Hansen, E. Haller, J. Farmer, V. Ozhogin, A. Rudnev, and A. Tikhomirov, J. Mater. Res. **8**, 1341 (1993).
[12] K. M. Itoh, J. Kato, M. Uemura, A. K. Kaliteevskii, O. N. Godisov, G. G. Devyatych, A. D. Bulanov, A. V. Gusev, I. D. Kovalev, P. G. Sennikov, H.-J. Pohl, N. V. Abrosimov, and H. Riemann, Jpn. J. Appl. Phys. **42**, 6248 (2003).
[13] D. V. Bulaev and D. Loss, Phys. Rev. Lett. **98**, 097202 (2007).
[14] C. Kloeffel, M. Trif, and D. Loss, Phys. Rev. B **84**, 195314 (2011).
[15] C. Kloeffel, M. Trif, P. Stano, and D. Loss, Phys. Rev. B **88**, 241405(R) (2013).
[16] S. Chesi, X. J. Wang, and W. Coish, The European Physical Journal Plus **129**, 86 (2014).
[17] A. Dobbie, M. Myronov, R. Morris, A. Hassan, M. Prest, V. Shah, E. Parker, T. Whall, and D. Leadley, Appl. Phys. Lett. **101**, 172108 (2012).
[18] A. Sammak, D. Sabbagh, N. W. Hendrickx, M. Lodari, B. Paquelet Wuetz, A. Tosato, L. Yeoh, M. Bollani, M. Virgilio, M. A. Schubert *et al.*, Adv. Funct. Mater. **29**, 1807613 (2019).
[19] M. Lodari, A. Tosato, D. Sabbagh, M. A. Schubert, G. Capellini, A. Sammak, M. Veldhorst, and G. Scappucci, Phys. Rev. B **100**, 041304(R) (2019).
[20] R. Winkler, *Spin-Orbit Coupling Effects in Two-Dimensional Electron and Hole Systems* (Springer, Berlin, Germany, 2003), Vol. 191.
[21] R. Winkler, D. Culcer, S. J. Papadakis, B. Habib, and M. Shayegan, Semicond. Sci. Technol. **23**, 114017 (2008).
[22] M. V. Durnev, M. M. Glazov, and E. L. Ivchenko, Phys. Rev. B **89**, 075430 (2014).
[23] E. Marcellina, A. R. Hamilton, R. Winkler, and D. Culcer, Phys. Rev. B **95**, 075305 (2017).
[24] E. Rashba and E. Sherman, Phys. Lett. A **129**, 175 (1988).
[25] R. Danneau, O. Klochan, W. R. Clarke, L. H. Ho, A. P. Micolich, M. Y. Simmons, A. R. Hamilton, M. Pepper, D. A. Ritchie, and U. Zülicke, Phys. Rev. Lett. **97**, 026403 (2006).
[26] D. S. Miserev and O. P. Sushkov, Phys. Rev. B **95**, 085431 (2017).
[27] J.-T. Hung, E. Marcellina, B. Wang, A. R. Hamilton, and D. Culcer, Phys. Rev. B **95**, 195316 (2017).
[28] J. H. Qvist and J. Danon, Phys. Rev. B **105**, 075303 (2022).
[29] J. C. Abadillo-Uriel, E. A. Rodríguez-Mena, B. Martinez, and Y.-M. Niquet, Phys. Rev. Lett. **131**, 097002 (2023).
[30] L. A. Terrazos, E. Marcellina, Z. Wang, S. N. Coppersmith, M. Friesen, A. R. Hamilton, X. Hu, B. Koiller, A. L. Saraiva, D. Culcer, R. B. Capaz, Phys. Rev. B **103**, 125201 (2021).
[31] Z. K. Keane, M. C. Godfrey, J. C. H. Chen, S. Fricke, O. Klochan, A. M. Burke, A. P. Micolich, H. E. Beere, D. A. Ritchie, K. V. Trunov, D. Reuter, A. D. Wieck, and A. R. Hamilton, Nano Lett. **11**, 3147 (2011).
[32] E. A. Chekhovich, A. B. Krysa, M. S. Skolnick, and A. I. Tartakovskii, Phys. Rev. Lett. **106**, 027402 (2011).
[33] D. Culcer, C. Lechner, and R. Winkler, Phys. Rev. Lett. **97**, 106601 (2006).

[34] H. Liu, E. Marcellina, A. R. Hamilton, and D. Culcer, Phys. Rev. Lett. **121**, 087701 (2018).

[35] J. C. Abadillo-Uriel, J. Salfi, X. Hu, S. Rogge, M. J. Calderon, and D. Culcer, Appl. Phys. Lett. **113**, 012102 (2018).

[36] J. H. Cullen, P. Bhalla, E. Marcellina, A. R. Hamilton, and D. Culcer, Phys. Rev. Lett. **126**, 256601 (2021).

[37] S. Roddaro, A. Fuhrer, P. Brusheim, C. Fasth, H. Q. Xu, L. Samuelson, J. Xiang, and C. M. Lieber, Phys. Rev. Lett. **101**, 186802 (2008).

[38] F. A. Zwanenburg, C. E. van Rijmenam, Y. Fang, C. M. Lieber, and L. P. Kouwenhoven, Nano Lett. **9**, 1071 (2009).

[39] R. Li, F. E. Hudson, A. S. Dzurak, and A. R. Hamilton, Nano Lett. **15**, 7314 (2015).

[40] S. Liles, R. Li, C. Yang, F. Hudson, M. Veldhorst, A. S. Dzurak, and A. Hamilton, Nat. Commun. **9**, 3255 (2018).

[41] Y. Hu, F. Kuemmeth, C. M. Lieber, and C. M. Marcus, Nat. Nanotechnol. **7**, 47 (2012).

[42] A. P. Higginbotham, T. W. Larsen, J. Yao, H. Yan, C. M. Lieber, C. M. Marcus, and F. Kuemmeth, Nano Lett. **14**, 3582 (2014).

[43] L. Vukušić, J. Kukučka, H. Watzinger, J. M. Milem, F. Schäffler, and G. Katsaros, Nano Lett. **18**, 7141 (2018).

[44] V. Pribiag, S. Nadj-Perge, S. Frolov, J. Van Den Berg, I. Van Weperen, S. Plissard, E. Bakkers, and L. Kouwenhoven, Nat. Nanotechnol. **8**, 170 (2013).

[45] N. Ares, G. Katsaros, V. N. Golovach, J. Zhang, A. Prager, L. I. Glazman, O. G. Schmidt, and S. De Franceschi, Appl. Phys. Lett. **103**, 263113 (2013).

[46] N. Ares, V. N. Golovach, G. Katsaros, M. Stoffel, F. Fournel, L. I. Glazman, O. G. Schmidt, and S. De Franceschi, Phys. Rev. Lett. **110**, 046602 (2013).

[47] M. Brauns, J. Ridderbos, A. Li, E. P. A. M. Bakkers, W. G. Van Der Wiel, and F. A. Zwanenburg, Phys. Rev. B **94**, 041411(R) (2016).

[48] H. Watzinger, C. Kloeffel, L. Vukusic, M. D. Rossell, V. Sessi, J. Kukucka, R. Kirchschlager, E. Lausecker, A. Truhlar, M. Glaser *et al.*, Nano Lett. **16**, 6879 (2016).

[49] B. Voisin, R. Maurand, S. Barraud, M. Vinet, X. Jehl, M. Sanquer, J. Renard, and S. De Franceschi, Nano Lett. **16**, 88 (2016).

[50] A. Srinivasan, K. L. Hudson, D. Miserev, L. A. Yeoh, O. Klochan, K. Muraki, Y. Hirayama, O. P. Sushkov, and A. R. Hamilton, Phys. Rev. B **94**, 041406(R) (2016).

[51] R. Mizokuchi, R. Maurand, F. Vigneau, M. Myronov, and S. De Franceschi, Nano Lett. **18**, 4861 (2018).

[52] E. Marcellina, A. Srinivasan, D. S. Miserev, O. P. Sushkov, D. Culcer, A. R. Hamilton, A. F. Croxall, D. A. Ritchie, I. Farrer, Phys. Rev. Lett. **121**, 077701 (2018).

[53] H. Wei, S. Mizoguchi, R. Mizokuchi, and T. Kodera, Jpn. J. Appl. Phys. **59**, SGGI10 (2020).

[54] T. Zhang, H. Liu, F. Gao, G. Xu, K. Wang, X. Zhang, G. Cao, T. Wang, J. Zhang, X. Hu *et al.*, Nano Lett. **21**, 3835 (2021).

[55] S. D. Liles, F. Martins, D. S. Miserev, A. A. Kiselev, I. D. Thorvaldson, M. J. Rendell, I. K. Jin, F. E. Hudson, M. Veldhorst, K. M. Itoh, O. P. Sushkov, T. D. Ladd, A. S. Dzurak, A. R. Hamilton, Phys. Rev. B **104**, 235303 (2021).

[56] H. Bohuslavskyi, D. Kotekar-Patil, R. Maurand, A. Corna, S. Barraud, L. Bourdet, L. Hutin, Y.-M. Niquet, X. Jehl, S. De Franceschi *et al.*, Appl. Phys. Lett. **109**, 193101 (2016).

[57] D. Q. Wang, O. Klochan, J.-T. Hung, D. Culcer, I. Farrer, D. A. Ritchie, and A. R. Hamilton, Nano Lett. **16**, 7685 (2016).

[58] J. van der Heijden, T. Kobayashi, M. G. House, J. Salfi, S. Barraud, R. Laviéville, M. Y. Simmons, and S. Rogge, Sci. Adv. **4**, eaat9199 (2018).

[59] R. Ezzouch, S. Zihlmann, V. P. Michal, J. Li, A. Apra, B. Bertrand, L. Hutin, M. Vinet, M. Urdampilleta, T. Meunier, X. Jehl, Y.-M. Niquet, M. Sanquer, S. DeFranceschi, and R. Maurand, Phys. Rev. Appl. **16**, 034031 (2021).

[60] R. Maurand, X. Jehl, D. Kotekar-Patil, A. Corna, H. Bohuslavskyi, R. Laviéville, L. Hutin, S. Barraud, M. Vinet, M. Sanquer *et al.*, Nat. Commun. **7**, 13575 (2016).

[61] H. Watzinger, J. Kukučka, L. Vukušić, F. Gao, T. Wang, F. Schäffler, J.-J. Zhang, and G. Katsaros, Nat. Commun. **9**, 3902 (2018).

[62] M. Lodari, N. W. Hendrickx, W. I. Lawrie, T.-K. Hsiao, L. M. Vandersypen, A. Sammak, M. Veldhorst, and G. Scappucci, Mater. Quantum. Technol. **1**, 011002 (2021).

[63] N. Hendrickx, W. Lawrie, L. Petit, A. Sammak, G. Scappucci, and M. Veldhorst, Nat. Commun. **11**, 3478 (2020).

[64] D. Jirovec, A. Hofmann, A. Ballabio, P. M. Mutter, G. Tavani, M. Botifoll, A. Crippa, J. Kukucka, O. Sagi, F. Martins *et al.*, Nat. Mater. **20**, 1106 (2021).

[65] N. Hendrickx, D. Franke, A. Sammak, G. Scappucci, and M. Veldhorst, Nature (London) **577**, 487 (2020).

[66] N. W. Hendrickx, W. I. Lawrie, M. Russ, F. van Riggelen, S. L. de Snoo, R. N. Schouten, A. Sammak, G. Scappucci, and M. Veldhorst, Nature (London) **591**, 580 (2021).

[67] F. N. M. Froning, M. J. Rančić, B. Hetényi, S. Bosco, M. K. Rehmann, A. Li, E. P. A. M. Bakkers, F. A. Zwanenburg, D. Loss, D. M. Zumbühl, F. R. Braakman, Phys. Rev. Res. **3**, 013081 (2021).

[68] K. Wang, G. Xu, F. Gao, H. Liu, R.-L. Ma, X. Zhang, Z. Wang, G. Cao, T. Wang, J.-J. Zhang *et al.*, Nat. Commun. **13**, 1 (2022).

[69] F. Gao, J.-H. Wang, H. Watzinger, H. Hu, M. J. Rančić, J.-Y. Zhang, T. Wang, Y. Yao, G.-L. Wang, J. Kukučka *et al.*, Adv. Mater. **32**, 1906523 (2020).

[70] H. Liu, T. Zhang, K. Wang, F. Gao, G. Xu, X. Zhang, S.-X. Li, G. Cao, T. Wang, J. Zhang, X. Hu, H.-O. Li, and G.-P. Guo, Phys. Rev. Appl. **17**, 044052 (2022).

[71] J. H. Ungerer, P. C. Kwon, T. Patlatiuk, J. Ridderbos, A. Kononov, D. Sarmah, E. P. A. M. Bakkers, D. Zumbuhl, and C. Schonenberger, Mater. Quantum. Technol. **3**, 031001 (2023).

[72] W. I. L. Lawrie, N. W. Hendrickx, F. van Riggelen, M. Russ, L. Petit, A. Sammak, G. Scappucci, and M. Veldhorst, Nano Lett. **20**, 7237 (2020).

[73] C.-A. Wang, C. Deprez, H. Tidjani, W. I. L. Lawrie, N. W. Hendrickx, A. Sammak, G. Scappucci, and M. Veldhorst, npj Quantum Information **9**, 58 (2023).

[74] F. Borsoi, N. W. Hendrickx, V. John, S. Motz, F. van Riggelen, A. Sammak, S. L. de Snoo, G. Scappucci, and M. Veldhorst, Nat. Nanotechnol. 1 (2023).

[75] N. Hendrickx, D. Franke, A. Sammak, M. Kouwenhoven, D. Sabbagh, L. Yeoh, R. Li, M. Tagliaferri, M. Virgilio, G. Capellini *et al.*, Nat. Commun. **9**, 2835 (2018).

[76] K. Aggarwal, A. Hofmann, D. Jirovec, I. Prieto, A. Sammak, M. Botifoll, S. Martí-Sánchez, M. Veldhorst, J. Arbiol, G. Scappucci, J. Danon, and G. Katsaros, Phys. Rev. Res. **3**, L022005 (2021).

[77] M. Valentini, O. Sagi, L. Baghumyan, T. de Gijsel, J. Jung, S. Calcaterra, A. Ballabio, J. A. Servin, K. Aggarwal, M. Janik *et al.*, arXiv:2306.07109.
[78] Y. Li, S.-X. Li, F. Gao, H.-O. Li, G. Xu, K. Wang, D. Liu, G. Cao, M. Xiao, T. Wang *et al.*, Nano Lett. **18**, 2091 (2018).
[79] G. Xu, Y. Li, F. Gao, H.-O. Li, H. Liu, K. Wang, G. Cao, T. Wang, J.-J. Zhang, G.-C. Guo *et al.*, New J. Phys. **22**, 083068 (2020).
[80] F. Vigneau, R. Mizokuchi, D. C. Zanuz, X. Huang, S. Tan, R. Maurand, S. Frolov, A. Sammak, G. Scappucci, F. Lefloch *et al.*, Nano Lett. **19**, 1023 (2019).
[81] J. Lidal and J. Danon, Phys. Rev. B **107**, 085303 (2023).
[82] T. Kobayashi, J. Salfi, C. Chua, J. van der Heijden, M. G. House, D. Culcer, W. D. Hutchison, B. C. Johnson, J. C. McCallum, H. Riemann *et al.*, Nat. Mater. **20**, 38 (2021).
[83] N. Piot, B. Brun, V. Schmitt, S. Zihlmann, V. Michal, A. Apra, J. Abadillo-Uriel, X. Jehl, B. Bertrand, H. Niebojewski *et al.*, Nat. Nanotechnol. **17**, 1072 (2022).
[84] J. Salfi, J. A. Mol, D. Culcer, and S. Rogge, Phys. Rev. Lett. **116**, 246801 (2016).
[85] J. Salfi, M. Tong, S. Rogge, and D. Culcer, Nanotechnol. **27**, 244001 (2016).
[86] C. Kloeffel, M. J. Rančić, and D. Loss, Phys. Rev. B **97**, 235422 (2018).
[87] Z. Wang, E. Marcellina, A. Hamilton, J. H. Cullen, S. Rogge, J. Salfi, D. Culcer *et al.*, npj Quantum Inf. **7**, 1 (2021).
[88] S. Bosco, B. Hetenyi, and D. Loss, PRX Quantum **2**, 010348 (2021).
[89] S. Bosco and D. Loss, Phys. Rev. Appl. **18**, 044038 (2022).
[90] C.-A. Wang, G. Scappucci, M. Veldhorst, and M. Russ, arXiv:2208.04795.
[91] O. Malkoc, P. Stano, and D. Loss, Phys. Rev. Lett. **129**, 247701 (2022).
[92] S. Geyer, B. Hetényi, S. Bosco, L. C. Camenzind, R. S. Eggli, A. Fuhrer, D. Loss, R. J. Warburton, D. M. Zumbuhl, and A. V. Kuhlmann, arXiv:2212.02308 1, 1 (2022).
[93] C. X. Yu, S. Zihlmann, J. C. Abadillo-Uriel, V. P. Michal, N. Rambal, H. Niebojewski, T. Bedecarrats, M. Vinet, E. Dumur, M. Filippone, B. Bertrand, S. D. Franceschi, Y.-M. Niquet, and R. Maurand, Nat. Nanotechnol. **18**, 741 (2023).
[94] N. Shimatani, Y. Yamaoka, R. Ishihara, A. Andreev, D. Williams, S. Oda, and T. Kodera, Appl. Phys. Lett. **117**, 094001 (2020).
[95] L. C. Camenzind, S. Geyer, A. Fuhrer, R. J. Warburton, D. M. Zumbuhl, and A. V. Kuhlmann, Nat. Electron **5**, 178 (2022).
[96] R. Winkler, Phys. Rev. B **70**, 125301 (2004).
[97] A. Ciocoiu, M. Khalifa, and J. Salfi, arXiv:2209.12026.
[98] B. Martinez, J. C. Abadillo-Uriel, E. A. Rodríguez-Mena, and Y.-M. Niquet, Phys. Rev. B **106**, 235426 (2022).
[99] S. Bosco, M. Benito, C. Adelsberger, and D. Loss, Phys. Rev. B **104**, 115425 (2021).
[100] C. Adelsberger, M. Benito, S. Bosco, J. Klinovaja, and D. Loss, Phys. Rev. B **105**, 075308 (2022).
[101] C. Adelsberger, S. Bosco, J. Klinovaja, and D. Loss, Phys. Rev. B **106**, 235408 (2022).
[102] M. Lodari, O. Kong, M. Rendell, A. Tosato, A. Sammak, M. Veldhorst, A. Hamilton, and G. Scappucci, Appl. Phys. Lett. **120**, 122104 (2022).
[103] L. E. Stehouwer, A. Tosato, D. D. Esposti, D. Costa, M. Veldhorst, A. Sammak, and G. Scappucci, Appl. Phys. Lett. **123**, 092101 (2023).
[104] C. Corley-Wiciak, C. Richter, M. H. Zoellner, I. Zaitsev, C. L. Manganelli, E. Zatterin, T. U. Schülli, A. A. Corley-Wiciak, J. Katzer, F. Reichmann *et al.*, ACS Appl. Mater. Interfaces **15**, 3119 (2023).
[105] J. Li, B. Venitucci, and Y.-M. Niquet, Phys. Rev. B **102**, 075415 (2020).
[106] J. Wortman and R. Evans, J. Appl. Phys. **36**, 153 (1965).
[107] G. Akhgar, L. Ley, D. L. Creedon, A. Stacey, J. C. McCallum, A. R. Hamilton, and C. I. Pakes, Phys. Rev. B **99**, 035159 (2019).
[108] D. S. Miserev, A. Srinivasan, O. A. Tkachenko, V. A. Tkachenko, I. Farrer, D. A. Ritchie, A. R. Hamilton, and O. P. Sushkov, Phys. Rev. Lett. **119**, 116803 (2017).
[109] V. Derakhshan Maman, M. F. Gonzalez-Zalba, and A. Pályi, Phys. Rev. Appl. **14**, 064024 (2020).
[110] D. Culcer, X. Hu, and S. Das Sarma, Appl. Phys. Lett. **95**, 073102 (2009).
[111] G. Ramon and Ł. Cywiński, Phys. Rev. B **105**, L041303 (2022).
[112] K. Roszak, D. Kwiatkowski, and Ł. Cywiński, Phys. Rev. A **100**, 022318 (2019).
[113] D. Culcer and N. M. Zimmerman, Appl. Phys. Lett. **102**, 232108 (2013).
[114] T. Lu, C. Harris, S.-H. Huang, Y. Chuang, J.-Y. Li, and C. Liu, Appl. Phys. Lett. **111**, 102108 (2017).
[115] B. Shalak, C. Delerue, and Y.-M. Niquet, Phys. Rev. B **107**, 125415 (2023).
[116] N. W. Hendrickx, L. Massai, M. Mergenthaler, F. Schupp, S. Paredes, S. W. Bedell, G. Salis, and A. Fuhrer, arXiv:2305.13150.
[117] M. Rendell, Spin dynamics of holes in GaAs and Ge semiconductor nanostructures, Ph.D. thesis, UNSW, Sydney, School of Physics UNSW, Sydney, 2021.